

Dynamic Network Regression

Yidong Zhou and Hans-Georg Müller

Department of Statistics, University of California, Davis

Davis, CA 95616, USA

September 2021

Abstract

Network data are increasingly available in various research fields, motivating statistical analysis for populations of networks where a network as a whole is viewed as a data point. Due to the non-Euclidean nature of networks, basic statistical tools available for scalar and vector data are no longer applicable when one aims to relate networks as outcomes to Euclidean covariates, while the study of how a network changes in dependence on covariates is often of paramount interest. This motivates to extend the notion of regression to the case of responses that are network data. Here we propose to adopt conditional Fréchet means implemented with both global least squares regression and local weighted least squares smoothing, extending the Fréchet regression concept to networks that are quantified by their graph Laplacians. The challenge is to characterize the space of graph Laplacians so as to justify the application of Fréchet regression. This characterization then leads to asymptotic rates of convergence for the corresponding M-estimators by applying empirical process methods. We demonstrate the usefulness and good practical performance of the proposed framework with simulations and with network data arising from NYC taxi records, as well as resting-state fMRI in neuroimaging.

KEY WORDS: Dynamic Networks, Euclidean Power Metric, Fréchet Regression, Graph Laplacians, Neuroimaging.

1 Introduction

Advances in modern science have led to the increasing availability of complex datasets that are non-Euclidean. Such “object-oriented data” (Wang and Marron 2007; Marron and Alonso 2014) or “random objects” (Müller 2016) can be viewed as random variables lying in a metric space where no Euclidean structure is available and only pairwise distances between the observed data can be defined. Recently, various kinds of non-Euclidean data, for example situated in a Riemannian manifold, such as in the space of covariance matrices (Dryden et al. 2009), or in more general metric spaces (Lyons 2013; Schötz 2020) have received increasing attention.

Due to the non-Euclidean nature of such object data, many classical notions of statistics such as population and sample means do not apply anymore and have to be modified. One of the earliest developments along these lines was the introduction of barycenters or Fréchet means to serve as generalization of centroids for random objects in general metric spaces (Fréchet 1948). The mathematical and statistical properties of Fréchet means have been widely studied for various metric spaces, including Riemannian manifolds, Wasserstein space of distributions, Kendall’s shape space, and Hadamard spaces (Bhattacharya and Patrangenaru 2003, 2005; Agueh and Carlier 2011; Huckemann 2012; Sturm 2003), where in the latter case existence and uniqueness is guaranteed without any further assumptions. Fréchet variance is a byproduct of Fréchet means and generalizes the usual notion of variance. It can be used to quantify the spread of distributions of metric-space valued random variables around their Fréchet means and is also useful for inference for metric space-valued data (Dubey and Müller 2019, 2020).

Data in social and biological sciences or civil engineering are often collected in the form of network data, where subjects or locations are represented in the form of nodes and similarities or connections between the nodes are represented by edges. Examples of network data include social networks (Knoke and Yang 2019), brain and gene networks (Wang et al. 2021) and transport networks (Von Ferber et al. 2009). The existing literature has mainly focused on the analysis of single networks, where the structural properties of a single network such as community structure are of interest. However, the increasing prevalence of network data comprising a collection of networks entails the need to develop statistical tools for populations of networks, often coupled with vector covariates, where each network is a data point. Such

data are encountered in the form of dynamic networks (Dubey and Müller 2021) and arise in the analysis of brain connectivity, traffic mobility, and many other areas.

Several recent studies focus on the analysis of a population of networks. For example, a geometric framework for inference concerning a population of networks was introduced and complemented by asymptotic theory for network averages in Ginestet et al. (2017) and Kolaczyk et al. (2020). A similar framework for studying populations of networks, where the graph space is viewed as the quotient space of a Euclidean space with respect to a finite group action was studied in Calissano et al. (2020).

A challenging and commonly encountered problem is to model the relationship between network objects and one or more explanatory variables, which corresponds to a regression problem. Instead of directly modeling the network objects, matrix representations of networks, such as the adjacency matrices and graph Laplacians, provide useful characterizations of the space of networks. A general framework for the statistical analysis of populations of labeled, undirected, weighted, and simple networks was developed by identifying networks with the corresponding graph Laplacians and embedding the space of graph Laplacians in a Euclidean feature-space, where statistical analysis including linear regression is carried out using extrinsic methods (Severn et al. 2019). Non-parametric regression for networks based on the same framework was proposed subsequently by adopting Nadaraya-Watson kernel estimators (Severn et al. 2021). However, embedding methods suffer from losing much of the relational information due to the non-Euclidean structure of the space of networks and assigning nonzero probability to points in the embedding space that do not represent networks. Another practical issue in this context is the need to estimate a covariance matrix which has a very large number of parameters, of the order of m^4 , where m is the number of nodes in the network.

Based on the adjacency matrix of a network, Calissano et al. (2021) proposed a network-valued regression model by implementing linear regression in the Euclidean space and then projecting back to the “graph space” through a quotient map (Calissano et al. 2020). This model is widely applicable for various kinds of unlabeled networks, but for the regression case there is no supporting theory and this approach may not be suitable for labeled networks, which are prevalent in applications. Examples include brain functional connectivity networks (Fornito et al. 2016), which are typically labeled as the goal is to study the role of different regions of

interest (ROIs) in brain activity.

To circumvent the problems of embedding methods and provide theoretical support for network-valued regression, we introduce a unifying intrinsic framework — Dynamic Network Regression (DNR) — by adopting conditional Fréchet means. Specifically, let $G = (V, E)$ be a network with a set of nodes V and a set of edge weights E . Under the assumption that G is labeled and simple (i.e., there are no self-loops or multi edges), one can uniquely associate each network G with its graph Laplacian L . Consider random pairs $(X, L) \sim F$, where X takes values in \mathbb{R}^p , L is a graph Laplacian and F indicates a suitable probability law. We investigate the dependence of L on covariates of interest X by adopting the general framework of Fréchet regression (Petersen and Müller 2019). The pointwise and uniform rates of convergence for corresponding M-estimators are obtained through a precise characterization of the space of graph Laplacians combined with empirical process methods.

We demonstrate the potential utility and flexibility of the proposed dynamic Network Regression (DNR) with New York taxi data and also with fMRI data obtained from the ADNI neuroimaging study. The New York taxi data give rise to transport networks that are constructed from yellow taxi records for the days from April 12, 2020 to September 30, 2020, along with covariates including COVID-19 information. The neuroimaging data reflect brain functional networks constructed from resting-state functional magnetic resonance imaging (rs-fMRI), where age of the subject is used as covariate.

The organization of this paper is as follows. In Section 2, we provide a precise characterization of the space of graph Laplacians, and discuss potential metrics for this space. The proposed Dynamic Network Regression (DNR) for network responses and vector covariates is introduced in Section 3. The pointwise and uniform rates of convergence for the estimators are established in Section 4. Computational details and simulation results for a sample of networks are presented in Section 5. The proposed framework is illustrated in Section 6 using the New York yellow taxi records and rs-fMRI data from the ADNI study. Detailed theoretical proofs and auxiliary results are in the Supplementary Material.

2 Preliminaries

2.1 Characterization of the space of graph Laplacians

Let $G_m = (V, E)$ be a network with a set of nodes $V = \{v_1, v_2, \dots, v_m\}$ and a set of edge weights $E = \{w_{ij} : w_{ij} \geq 0, 1 \leq i, j \leq m\}$, where $w_{ij} = 0$ indicates v_i and v_j are unconnected. Some basic and mild restrictions on the networks G_m we consider here are as follows.

(A0) G_m is simple, i.e., no self-loops or multi-edges.

(A1) G_m is weighted, undirected, and labeled.

(A2) The edge weights w_{ij} are bounded above by $W \geq 0$, i.e., $0 \leq w_{ij} \leq W$.

Assumption (A0) is required for the one-to-one correspondence between a network G_m and its graph Laplacian, which is our central tool to represent networks. Assumption (A1) guarantees that the adjacency matrix $A = \{w_{ij}\}$ is symmetric, i.e., $w_{ij} = w_{ji}$ for all i, j , which is necessary for our theoretical developments. Assumption (A2) puts a limit on the maximum strength of the connection between two nodes and prevents extremes. Any network satisfying assumptions (A0)–(A2) can be uniquely associated with its graph Laplacian $L = (l_{ij})$, defined as

$$l_{ij} = \begin{cases} -w_{ij}, & i \neq j \\ \sum_{k \neq i} w_{ik}, & i = j \end{cases}$$

for $1 \leq i, j \leq m$, which motivates to characterize the space of networks through the corresponding space of graph Laplacians given by

$$\mathcal{L}_m = \{L = (l_{ij}) : L = L'; L1_m = 0_m; -W \leq l_{ij} \leq 0 \text{ for } i \neq j\}, \quad (1)$$

where 1_m and 0_m are the m -vectors of ones and zeroes, respectively. For every $L \in \mathcal{L}_m$,

(P0) $L' = L$,

(P1) the entries in each row sum to 0, $L1_m = 0_m$,

(P2) the off-diagonal entries are nonpositive and bounded below, $-W \leq l_{ij} \leq 0$.

Another well-known property of graph Laplacians is their positive semi-definiteness, $x' L x \geq 0$ for all $x \in \mathbb{R}^m$, which immediately follows from properties (P0)-(P2), as any such L is diagonally dominant, i.e., $l_{ii} = \sum_{j \neq i} |l_{ij}|$ (De Klerk 2006, Page 232).

A precise geometric characterization of the space of graph Laplacians can be found in Ginestet et al. (2017). The characterizations in this paper were however limited to the case of graph Laplacians with fixed rank, which is not practicable when considering network-valued regression where the rank can change in dependence on predictor levels. This necessitates and motivates study of the space of graph Laplacians with no restrictions on their rank in the following.

Proposition 1. *The space \mathcal{L}_m , defined in (1), is a bounded, closed, and convex subset in \mathbb{R}^{m^2} of dimension $m(m - 1)/2$.*

All proofs are given in the Supplementary Material. Proposition 1 ensures the existence and uniqueness of projections onto \mathcal{L}_m that we will utilize in the proposed regression approach.

2.2 Choice of metrics

One can adopt one of several metrics when viewing the space of graph Laplacians \mathcal{L}_m as a metric space. A common choice is the Frobenius metric, defined as

$$d_F(L_1, L_2) = \|L_1 - L_2\|_F = \{\text{trace}((L_1 - L_2)'(L_1 - L_2))\}^{\frac{1}{2}}, \quad (2)$$

which is simply the Euclidean metric if the matrix is stretched to a long vector of length m^2 . We will refer to d_F as the Euclidean metric for simplicity. While d_F is the simplest of the possible metrics on the space of graph Laplacians, it is not necessarily the most appropriate metric, depending on the specific application setting. A downside of the metric d_F is that the determinant typically inflates along geodesics, which is undesirable and is referred to as the swelling phenomenon (Arsigny et al. 2007; Lin 2019).

Several non-Euclidean metrics have been proposed as alternatives to d_F . Denote the space of real symmetric positive semi-definite $m \times m$ matrices by \mathcal{S}_m^+ . Note that the space of graph Laplacians \mathcal{L}_m is a subset of \mathcal{S}_m^+ . Let $U \Lambda U'$ be the usual spectral decomposition of $S \in \mathcal{S}_m^+$, with $U \in \mathcal{O}_m$ an orthogonal matrix and Λ diagonal with non-negative entries. Defining matrix

power maps

$$F_\alpha(S) = S^\alpha = U\Lambda^\alpha U' : \mathcal{S}_m^+ \mapsto \mathcal{S}_m^+, \quad (3)$$

where the power $\alpha > 0$ is a constant and noting that F_α is bijective with inverse $F_{1/\alpha}$, the Euclidean power metric (Dryden et al. 2009) between graph Laplacians is

$$d_{F,\alpha}(L_1, L_2) = d_F(F_\alpha(L_1), F_\alpha(L_2)). \quad (4)$$

For $\alpha = 1$, $d_{F,\alpha}$ reduces to the Euclidean metric d_F . For larger α there is more emphasis on larger entries of graph Laplacians, while for small α large and small entries are treated more evenly and there is less sensitivity to outliers. In particular, $d_{F,\alpha}$ with $0 < \alpha < 1$ is associated with a reduced swelling effect, while $d_{F,\alpha}$ with $\alpha > 1$ in contrast will amplify it and thus often will be unfavorable. For $\alpha = 1/2$ the Euclidean square root metric $d_{F,1/2}$ is a canonical choice that has been widely studied (Dryden et al. 2009, 2010; Zhou et al. 2016; Severn et al. 2019; Tavakoli et al. 2019). For example, Dryden et al. (2010) studied different values of α in the context of diffusion tensor imaging and ended up with the choice $\alpha = 1/2$; also Tavakoli et al. (2019) illustrated the advantages of using $d_{F,1/2}$ through a spatial modeling approach for linguistic object data. In our applications, we likewise focus on the Euclidean square root metric due to its promising properties and compare its performance with the Euclidean metric d_F ; see also Petersen and Müller (2016) regarding the choice of α .

Another non-Euclidean metric arising from the area of shape analysis, the Procrustes metric, has recently received some attention (Dryden and Mardia 2016). Formally, the Procrustes metric is defined as

$$d_P(L_1, L_2) = \inf_{R \in \mathcal{O}_m} \|L_1 - L_2 R\|_F, \quad (5)$$

where R is an orthogonal matrix, and involves matching L_2 optimally to L_1 by rotation and reflection. Since graph Laplacians are all centered, applying the Procrustes metric only preserves the scale information (Dryden and Mardia 2016, Chapter 5). However, removal of rotation and reflection information for graph Laplacians is not desirable, as nodes may be relabelled or combined in the Procrustes matching step, which is a problem when the focus is on labeled networks as in this paper. We therefore do not consider this metric further.

3 Dynamic Network Regression

Consider a random object $Y \sim F_Y$ taking values in a metric space (Ω, d) . Under appropriate conditions, the Fréchet mean and Fréchet variance of random objects in metric spaces (Fréchet 1948), as generalizations of usual notions of mean and variance, are defined as

$$\omega_{\oplus} = \operatorname{argmin}_{\omega \in \Omega} E[d^2(Y, \omega)], \quad V_{\oplus} = E[d^2(Y, \omega_{\oplus})], \quad (6)$$

where the existence and uniqueness of the minimizer depends on structural properties of the underlying metric space, and is guaranteed for Hadamard spaces. A general approach for regression of metric space-valued responses on Euclidean predictors, referred to as Fréchet regression, was proposed by extending Fréchet means to conditional Fréchet means which can be implemented in terms of generalizations of both linear and local linear regression (Petersen and Müller 2019). Adopting the general framework of this approach, our goal is to model regression relationships between responses which are \mathcal{L}_m -valued, i.e. graph Laplacians of fixed dimension m , and vectors of real-valued predictors. Equipped with a proper metric d , \mathcal{L}_m becomes a metric space (\mathcal{L}_m, d) , and an analysis of the properties of this space will be the key to establish theoretical support for the proposed Dynamic Network Regression (DNR) models.

Suppose $(X, L) \sim F$ is a random pair, where X and L take values in \mathbb{R}^p and $\mathcal{L}_m \equiv (\mathcal{L}_m, d)$, respectively, and F is the joint distribution of (X, L) on $\mathbb{R}^p \times \mathcal{L}_m$. We denote the marginal distributions of X and L as F_X and F_L , respectively, and assume that $\mu = E(X)$ and $\Sigma = \operatorname{Var}(X)$ exist, with Σ positive definite. The conditional distributions $F_{X|L}$ and $F_{L|X}$ are also assumed to exist. The conditional Fréchet mean, which corresponds to the regression function of L given $X = x$, is

$$m(x) = \operatorname{argmin}_{\omega \in \mathcal{L}_m} M(\omega, x), \quad M(\cdot, x) = E[d^2(L, \cdot) | X = x], \quad (7)$$

where $M(\cdot, x)$ is referred to as the conditional Fréchet function. Further suppose that $(X_k, L_k) \sim F$, $k = 1, 2, \dots, n$ are independent and define

$$\bar{X} = n^{-1} \sum_{k=1}^n X_k, \quad \hat{\Sigma} = n^{-1} \sum_{k=1}^n (X_k - \bar{X})(X_k - \bar{X})'$$

The global DNR given $X = x$ is defined as

$$m_G(x) = \operatorname{argmin}_{\omega \in \mathcal{L}_m} M_G(\omega, x), \quad M_G(\cdot, x) = E[s_G(x) d^2(L, \cdot)], \quad (8)$$

where $s_G(x) = 1 + (X - \mu)' \Sigma^{-1} (x - \mu)$. The corresponding sample version is

$$\hat{m}_G(x) = \operatorname{argmin}_{\omega \in \mathcal{L}_m} \hat{M}_G(\omega, x), \quad \hat{M}_G(\cdot, x) = \frac{1}{n} \sum_{k=1}^n s_{kG}(x) d^2(L_k, \cdot), \quad (9)$$

where $s_{kG}(x) = 1 + (X_k - \bar{X})' \hat{\Sigma}^{-1} (x - \bar{X})$.

For local DNR, we present details only for the case of a scalar predictor $X \in \mathbb{R}$, where the extension to $X \in \mathbb{R}^p$ with $p > 1$ is straightforward while estimates will be subject to the curse of dimensionality. Consider a smoothing kernel $K(\cdot)$ corresponding to a probability density and $K_h(\cdot) = h^{-1} K(\cdot/h)$ with h a bandwidth. The local DNR given $X = x$ can be written as

$$m_{L,h}(x) = \operatorname{argmin}_{\omega \in \mathcal{L}_m} M_{L,h}(\omega, x), \quad M_{L,h}(\cdot, x) = E[s_L(x, h) d^2(L, \cdot)], \quad (10)$$

where $s_L(x, h) = \frac{1}{\sigma_0^2} K_h(X - x) [\mu_2 - \mu_1(X - x)]$ with $\mu_j = E[K_h(X - x)(X - x)^j]$ for $j = 0, 1, 2$ and $\sigma_0^2 = \mu_0 \mu_2 - \mu_1^2$. The corresponding sample version is

$$\hat{m}_{L,n}(x) = \operatorname{argmin}_{\omega \in \mathcal{L}_m} \hat{M}_{L,n}(\omega, x), \quad \hat{M}_{L,n}(\cdot, x) = \frac{1}{n} \sum_{k=1}^n s_{kL}(x, h) d^2(L_k, \cdot). \quad (11)$$

Here $s_{kL}(x, h) = \frac{1}{\hat{\sigma}_0^2} K_h(X_k - x) [\hat{\mu}_2 - \hat{\mu}_1(X_k - x)]$, where $\hat{\mu}_j = n^{-1} \sum_{k=1}^n K_h(X_k - x)(X_k - x)^j$ for $j = 0, 1, 2$ and $\hat{\sigma}_0^2 = \hat{\mu}_0 \hat{\mu}_2 - \hat{\mu}_1^2$. The dependency on n is through the bandwidth sequence $h = h_n$.

We note that for the case where $X \in \mathbb{R}^p$ with $p > 1$, the weight function takes a slightly different form,

$$s_L(x, h) = \frac{1}{\mu_0 - \mu_1' \mu_2^{-1} \mu_1} K_h(X - x) [1 - \mu_1' \mu_2^{-1} (X - x)],$$

where $\mu_0 = E[K_h(X - x)]$, $\mu_1 = E[K_h(X - x)(X - x)]$, and $\mu_2 = E[K_h(X - x)(X - x)(X - x)']$ is non-degenerate. The sample version $s_{kL}(x, h)$ can be defined similarly. While the global DNR relies on stronger model assumptions, it does not require a tuning parameter and is applicable for categorical predictors. The local DNR, by contrast, is more flexible as long as the regression relation is smooth, the covariate dimension is low and covariates are continuous.

4 Asymptotic Properties

In this section, we establish consistency of both global and local DNR estimators as per (9) and (11) using the metrics of interest introduced in Section 2.2. Both pointwise and uniform rates

of convergence are obtained under the framework of M-estimation. These rates are validated by simulations in Section 5, where we find that the finite sample results are entirely consistent with theory (see Figure 3). We first consider the case where \mathcal{L}_m is endowed with the Euclidean metric d_F . As a subset of \mathbb{R}^{m^2} , \mathcal{L}_m inherits a natural metric from \mathbb{R}^{m^2} , which coincides with d_F . The convexity and closedness of \mathcal{L}_m imply that the minimizers $\hat{m}_G(x)$ and $\hat{m}_{L,n}(x)$ defined in (9) and (11) exist and are unique for any x . The following result formalizes the consistency of the proposed global DNR estimator and provides rates of convergence.

Theorem 1. *Let the space of graph Laplacians \mathcal{L}_m be endowed with the Euclidean metric d_F . Then for a fixed $x \in \mathbb{R}^p$, it holds for $m_G(x)$ and $\hat{m}_G(x)$ as per (8) and (9) that*

$$d_F(m_G(x), \hat{m}_G(x)) = O_P(n^{-\frac{1}{2}}). \quad (12)$$

Furthermore, for a given $B > 0$,

$$\sup_{\|x\|_E \leq B} d_F(m_G(x), \hat{m}_G(x)) = O_P(n^{-\frac{1}{2(1+\varepsilon)}}), \quad (13)$$

for any $\varepsilon > 0$.

As in the Euclidean case where one needs to consider bias in exchange for greater flexibility for non-parametric approaches, the rate of convergence for local DNR estimator depends both on bias $d_F(m(x), m_{L,h}(x))$ and stochastic deviation $d_F(m_{L,h}(x), \hat{m}_{L,n}(x))$; see the following result.

Theorem 2. *Let the space of graph Laplacians \mathcal{L}_m be endowed with the Euclidean metric d_F . Suppose (LP0), (LP1) hold, then for a fixed $x \in \mathbb{R}$, it holds for $m(x)$, $m_{L,h}(x)$, and $\hat{m}_{L,n}(x)$ as per (7), (10), and (11), respectively that*

$$d_F(m(x), m_{L,h}(x)) = O(h^2), \quad (14)$$

$$d_F(m_{L,h}(x), \hat{m}_{L,n}(x)) = O_P((nh)^{-\frac{1}{2}}). \quad (15)$$

With $h \sim n^{-1/5}$, it holds that

$$d_F(m(x), \hat{m}_{L,n}(x)) = O_P(n^{-\frac{2}{5}}). \quad (16)$$

Furthermore, suppose (LU0), (LU1) hold, for a given closed interval \mathcal{T} , if $h \rightarrow 0$, $nh^2(-\log h)^{-1} \rightarrow \infty$ as $n \rightarrow \infty$, then for any $\varepsilon > 0$,

$$\sup_{x \in \mathcal{T}} d_F(m(x), m_{L,h}(x)) = O(h^2), \quad (17)$$

$$\sup_{x \in \mathcal{T}} d_F(m_{L,h}(x), \hat{m}_{L,n}(x)) = O_P(\max\{(nh^2)^{-\frac{1}{2+\varepsilon}}, (nh^2(-\log h)^{-1})^{-\frac{1}{2}}\}). \quad (18)$$

With $h \sim n^{-1/(6+2\varepsilon)}$, it holds that

$$\sup_{x \in \mathcal{T}} d_F(m(x), \hat{m}_{L,n}(x)) = O_P(n^{-\frac{1}{3+\varepsilon}}). \quad (19)$$

The proof of Theorem 1 and Theorem 2 relies on the fact that \mathcal{L}_m is convex, bounded, and of finite dimension. We represent global and local DNRs as projections $P_{\mathcal{L}_m}$ onto \mathcal{L}_m ,

$$m_G(x) = \operatorname{argmin}_{\omega \in \mathcal{L}_m} d_F^2(B_G(x), \omega) = P_{\mathcal{L}_m}(B_G(x)), \quad (20)$$

$$m_{L,h}(x) = \operatorname{argmin}_{\omega \in \mathcal{L}_m} d_F^2(B_{L,h}(x), \omega) = P_{\mathcal{L}_m}(B_{L,h}(x)), \quad (21)$$

where $B_G(x) = E[s_G(x)L]$ and $B_{L,h}(x) = E[s_L(x,h)L]$. The corresponding sample versions are

$$\hat{m}_G(x) = \operatorname{argmin}_{\omega \in \mathcal{L}_m} d_F^2(\hat{B}_G(x), \omega) = P_{\mathcal{L}_m}(\hat{B}_G(x)), \quad (22)$$

$$\hat{m}_{L,n}(x) = \operatorname{argmin}_{\omega \in \mathcal{L}_m} d_F^2(\hat{B}_{L,n}(x), \omega) = P_{\mathcal{L}_m}(\hat{B}_{L,n}(x)), \quad (23)$$

where $\hat{B}_G(x) = n^{-1} \sum_{k=1}^n s_{kG}(x)L_k$ and $\hat{B}_{L,n}(x) = n^{-1} \sum_{k=1}^n s_{kL}(x,h)L_k$.

We now turn our attention to the Euclidean power metric $d_{F,\alpha}$. Recall that the graph Laplacian L is centered and the off-diagonal entries are bounded by W as per (1). By the equivalence of the Frobenius norm and the l_2 -operator norm in \mathbb{R}^{m^2} , it immediately follows that the largest eigenvalue of L is bounded, say by C , a nonnegative constant depending on m and W . Define the embedding space \mathcal{M}_m to be a subset of \mathcal{S}_m^+ ,

$$\mathcal{M}_m = \{S \in \mathcal{S}_m^+ : \lambda_1(S) \leq C^\alpha\}, \quad (24)$$

where $\lambda_1(S)$ is the largest eigenvalue of S . Note that the image of \mathcal{L}_m under the matrix power map F_α , i.e., $F_\alpha(\mathcal{L}_m)$, is a subset of \mathcal{M}_m as a consequence of the bound C on the largest eigenvalue of each graph Laplacian.

After applying the matrix power map F_α , the image of \mathcal{L}_m is embedded in \mathcal{M}_m , where DNR is carried out using the Euclidean metric d_F . When transforming back from the embedding

space \mathcal{M}_m to \mathcal{L}_m , we first apply the inverse matrix power map $F_{1/\alpha}$ and then a projection $P_{\mathcal{L}_m}$ onto \mathcal{L}_m . The general idea involving embedding, mapping and projections is shown schematically in Figure 1.

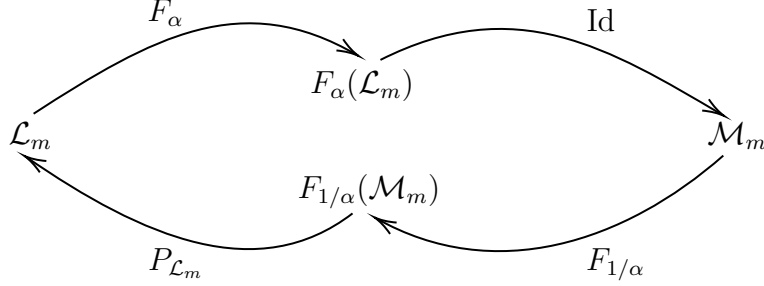


Figure 1: Schematic diagram for the Euclidean power metric $d_{F,\alpha}$. \mathcal{L}_m and \mathcal{M}_m are the space of graph Laplacians and the embedding space defined in (1) and (24), respectively. DNR is carried out using the Euclidean metric d_F in the embedding space \mathcal{M}_m . F_α is the matrix power map defined in (3), with $F_{1/\alpha}$ being its inverse. $F_\alpha(\mathcal{L}_m)$ is the image of \mathcal{L}_m under F_α and $F_{1/\alpha}(\mathcal{M}_m)$ is the image of \mathcal{M}_m under $F_{1/\alpha}$. The identity map is denoted by Id, which embeds $F_\alpha(\mathcal{L}_m)$ in the embedding space \mathcal{M}_m . $P_{\mathcal{L}_m}$ is the projection onto \mathcal{L}_m .

The global DNR in the embedding space \mathcal{M}_m using the Euclidean metric d_F can be likewise simplified to be a projection $P_{\mathcal{M}_m}$ onto \mathcal{M}_m ,

$$m_G^\alpha(x) = \operatorname{argmin}_{\omega \in \mathcal{M}_m} d_F^2(B_G^\alpha(x), \omega) = P_{\mathcal{M}_m}(B_G^\alpha(x)), \quad (25)$$

where $B_G^\alpha(x) = E[s_G(x)F_\alpha(L)]$. Then the global DNR in the space of graph Laplacians \mathcal{L}_m using the Euclidean power metric $d_{F,\alpha}$ is obtained by applying the inverse matrix power map $F_{1/\alpha}$ and a projection $P_{\mathcal{L}_m}$ successively on $m_G^\alpha(x)$. That is (with a slight abuse of notation)

$$m_G(x) = \operatorname{argmin}_{\omega \in \mathcal{L}_m} d_F^2(F_{1/\alpha}(m_G^\alpha(x)), \omega) = P_{\mathcal{L}_m}(F_{1/\alpha}(m_G^\alpha(x))). \quad (26)$$

The corresponding sample versions are

$$\hat{m}_G^\alpha(x) = \operatorname{argmin}_{\omega \in \mathcal{M}_m} d_F^2(\hat{B}_G^\alpha(x), \omega) = P_{\mathcal{M}_m}(\hat{B}_G^\alpha(x)), \quad (27)$$

$$\hat{m}_G(x) = \operatorname{argmin}_{\omega \in \mathcal{L}_m} d_F^2(F_{1/\alpha}(\hat{m}_G^\alpha(x)), \omega) = P_{\mathcal{L}_m}(F_{1/\alpha}(\hat{m}_G^\alpha(x))), \quad (28)$$

where $\hat{B}_G^\alpha(x) = n^{-1} \sum_{k=1}^n s_{kG}(x)F_\alpha(L_k)$. Similarly for the local DNR,

$$m(x) = P_{\mathcal{L}_m}(F_{1/\alpha}(P_{\mathcal{M}_m}(B^\alpha(x))), \quad (29)$$

$$m_{L,h}(x) = P_{\mathcal{L}_m}(F_{1/\alpha}(P_{\mathcal{M}_m}(B_{L,h}^\alpha(x))), \quad (30)$$

$$\hat{m}_{L,n}(x) = P_{\mathcal{L}_m}(F_{1/\alpha}(P_{\mathcal{M}_m}(\hat{B}_{L,n}^\alpha(x))), \quad (31)$$

where $B^\alpha(x) = E[F_\alpha(L)|X = x]$, $B_{L,h}^\alpha(x) = E[s_L(x, h)F_\alpha(L)]$ and $\hat{B}_{L,n}^\alpha(x) = n^{-1} \sum_{k=1}^n s_{kL}(x, h)F_\alpha(L_k)$.

To obtain rates of convergence for power metrics $d_{F,\alpha}$, we need the following proposition concerning the Hölder continuity of the matrix power map F_α . Suppose that U is a set in \mathbb{R}^{n_1} , E is a non-empty subset of U , and $0 < \beta \leq 1$. A function $g : U \mapsto \mathbb{R}^{n_2}$ is uniformly Hölder continuous with exponent β and Hölder coefficient H in the set E , shortly (β, H) -Hölder continuous, if there exists $H \geq 0$ such that

$$\|g(x) - g(y)\|_F \leq H\|x - y\|_F^\beta, \quad \text{for all } x, y \in E. \quad (32)$$

For $\beta = 1$ the function g is said to be Lipschitz continuous in E with Lipschitz constant H , shortly H -Lipschitz continuous.

Proposition 2. Define $\mathcal{E}_m = \{S \in \mathcal{S}_m^+ : \lambda_1(S) \leq C\}$, where $\lambda_1(S)$ is the largest eigenvalue of S and $C \geq 0$ is a constant. Then the matrix power map F_α as per (3) is

- (1) $(\alpha, m^{(1-\alpha)/2})$ -Hölder continuous in \mathcal{S}_m^+ for $0 < \alpha < 1$;
- (2) $\alpha C^{\alpha-1}$ -Lipschitz continuous in \mathcal{E}_m for $\alpha \geq 1$.

Proposition 2 leads to rate of convergence results for the global and local DNR estimators defined in (28) and (31), where the population targets for the global and local DNR under the Euclidean power metric $d_{F,\alpha}$ are defined in (26) and (29).

Theorem 3. If the space of graph Laplacians \mathcal{L}_m is endowed with the Euclidean power metric $d_{F,\alpha}$, for any fixed $x \in \mathbb{R}^p$, it holds for $m_G(x)$ and $\hat{m}_G(x)$ as per (26) and (28) that

$$d_F(m_G(x), \hat{m}_G(x)) = \begin{cases} O_P(n^{-\frac{1}{2}}) & 0 < \alpha \leq 1 \\ O_P(n^{-\frac{1}{2\alpha}}) & \alpha > 1 \end{cases}. \quad (33)$$

Furthermore, for a given $B > 0$,

$$\sup_{\|x\|_E \leq B} d_F(m_G(x), \hat{m}_G(x)) = \begin{cases} O_P(n^{-\frac{1}{2(1+\varepsilon)}}) & 0 < \alpha \leq 1 \\ O_P(n^{-\frac{1}{2\alpha(1+\varepsilon)}}) & \alpha > 1 \end{cases}, \quad (34)$$

for any $\varepsilon > 0$.

Theorem 4. Suppose the space of graph Laplacians \mathcal{L}_m is endowed with the Euclidean power metric $d_{F,\alpha}$. Under (LP0), (LP1), for a fixed $x \in \mathbb{R}$, it holds for $m(x)$, $m_{L,h}(x)$, and $\hat{m}_{L,n}(x)$ as per (29), (30), and (31), respectively, that

$$d_F(m(x), m_{L,h}(x)) = \begin{cases} O(h^2) & 0 < \alpha \leq 1 \\ O(h^{\frac{2}{\alpha}}) & \alpha > 1 \end{cases}, \quad (35)$$

$$d_F(m_{L,h}(x), \hat{m}_{L,n}(x)) = \begin{cases} O_P((nh)^{-\frac{1}{2}}) & 0 < \alpha \leq 1 \\ O_P((nh)^{-\frac{1}{2\alpha}}) & \alpha > 1 \end{cases}. \quad (36)$$

With $h \sim n^{-1/5}$, it holds that

$$d_F(m(x), \hat{m}_{L,n}(x)) = \begin{cases} O_P(n^{-\frac{2}{5}}) & 0 < \alpha \leq 1 \\ O_P(n^{-\frac{2}{5\alpha}}) & \alpha > 1 \end{cases}. \quad (37)$$

Furthermore, under (LU0), (LU1), for a given closed interval \mathcal{T} , if $h \rightarrow 0$, $nh^2(-\log h)^{-1} \rightarrow \infty$ as $n \rightarrow \infty$, for any $\varepsilon > 0$,

$$\sup_{x \in \mathcal{T}} d_F(m(x), m_{L,h}(x)) = \begin{cases} O(h^2) & 0 < \alpha \leq 1 \\ O(h^{\frac{2}{\alpha}}) & \alpha > 1 \end{cases}, \quad (38)$$

$$\begin{aligned} \sup_{x \in \mathcal{T}} d_F(m_{L,h}(x), \hat{m}_{L,n}(x)) = \\ \begin{cases} O_P(\max\{(nh^2)^{-\frac{1}{2+\varepsilon}}, (nh^2(-\log h)^{-1})^{-\frac{1}{2}}\}) & 0 < \alpha \leq 1 \\ O_P(\max\{(nh^2)^{-\frac{1}{\alpha(2+\varepsilon)}}, (nh^2(-\log h)^{-1})^{-\frac{1}{2\alpha}}\}) & \alpha > 1 \end{cases}. \end{aligned} \quad (39)$$

With $h \sim n^{-1/(6+2\varepsilon)}$, it holds that

$$\sup_{x \in \mathcal{T}} d_F(m(x), \hat{m}_{L,n}(x)) = \begin{cases} O_P(n^{-\frac{1}{3+\varepsilon}}) & 0 < \alpha \leq 1 \\ O_P(n^{-\frac{1}{\alpha(3+\varepsilon)}}) & \alpha > 1 \end{cases}. \quad (40)$$

For the Euclidean power metric $d_{F,\alpha}$, rates of convergence for both the global and local DNR depend on the choice of power α . Specifically, rates of convergence are the same as those for the Euclidean metric d_F if $0 < \alpha < 1$, providing theoretical justification for the use of the Euclidean power metric with $0 < \alpha < 1$.

We note that the convexity of the target space is crucial in the proof of existence and uniqueness for the minimizers in (7)–(11). Indeed, as stated in Deutsch (2012, Chapter 12), every Chebyshev subset of a finite-dimensional Hilbert space is convex. Let U be a nonempty subset of the Hilbert space X , then U is called a Chebyshev subset if each $x \in X$ has exactly one best approximation in U . It can be shown that $F_\alpha(\mathcal{L}_m)$ as a subset of \mathbb{R}^{m^2} is not convex, implying that it is not a Chebyshev subset. Hence uniqueness for the minimizers in (7)–(11) cannot be guaranteed. For this reason, we include embedding $F_\alpha(\mathcal{L}_m)$ in \mathcal{M}_m as defined in (24), where uniqueness for the minimizers in (7)–(11) can be ensured.

5 Implementation and Simulations

Implementation of the proposed method involves two projections $P_{\mathcal{L}_m}$ and $P_{\mathcal{M}_m}$ as mentioned in Section 4. Due to the convexity and closeness of \mathcal{L}_m and \mathcal{M}_m , $P_{\mathcal{L}_m}$ and $P_{\mathcal{M}_m}$ exist and are unique. To implement $P_{\mathcal{L}_m}(B)$ where $B = (b_{ij})$ is a constant $m \times m$ matrix, one needs to solve the following optimization problem,

$$\begin{aligned}
\text{minimize} \quad & f(L) = d_F^2(B, L) = \sum_{i=1}^m \sum_{j=1}^m (b_{ij} - l_{ij})^2 \\
\text{subject to} \quad & l_{ij} - l_{ji} = 0, \quad 1 \leq i, j \leq m, \\
& \sum_{j=1}^m l_{ij} = 0, \quad 1 \leq i \leq m, \\
& -W \leq l_{ij} \leq 0, \quad 1 \leq i \neq j \leq m,
\end{aligned} \tag{41}$$

where $L = (l_{ij})$ is a graph Laplacian. The objective function $f(L)$ is convex quadratic since its Hessian $2I_{m^2}$ is strictly positive definite. The three constraints, corresponding to the three properties (P0)–(P2) of graph Laplacians, are all linear. It immediately follows that (41) is a convex quadratic optimization problem, which can be solved using quadratic programming. We use the `osqp` (Stellato et al. 2020) package in R (R Core Team 2021) to solve this optimization problem.

Note that \mathcal{M}_m is a bounded subset of the positive semi-definite cone \mathcal{S}_m^+ . To implement $P_{\mathcal{M}_m}$, we first take the projection onto \mathcal{S}_m^+ and then truncate the eigenvalues to ensure that the largest eigenvalue is less than or equal to C^α . The projection $P_{\mathcal{S}_m^+}$ onto \mathcal{S}_m^+ is straightforward and

has been studied in [Boyd et al. \(2004, Chapter 8, Page 399\)](#). The unique solution for $P_{\mathcal{S}_m^+}(B)$ is $\sum_{i=1}^m \max\{0, \lambda_i\} v_i v_i'$, where $B = \sum_{i=1}^m \lambda_i v_i v_i'$ is the spectral decomposition of a constant $m \times m$ symmetric matrix B .

To assess the performance of the global and local DNR estimates in (9) and (11) through simulations, we need to devise a generative model. Denote the half vectorization excluding the diagonal of a symmetric and centered matrix by vech , with inverse operation being vech^{-1} . By the symmetry and centrality as per properties (P0) and (P1), every graph Laplacian L is fully determined by its upper (or lower) triangle part, which can be further vectorized into $\text{vech}(L)$ — a vector of length $d := m(m-1)/2$. We hence can construct the conditional distributions $F_{L|X}$ by assigning an independent beta distribution to each element of $\text{vech}(L)$. Specifically, a random sample of size d , $(\beta_1, \dots, \beta_d)$, is generated using beta distributions whose parameters depend on the scalar predictor X and vary under different simulation scenarios. The random response L is then generated conditional on X through an inverse half vectorization vech^{-1} on $(-\beta_1, \dots, -\beta_d)$. Four different simulation scenarios involving different types of regression and different metrics are illustrated in [Table 1](#).

The space of graph Laplacians \mathcal{L}_m is not a vector space. Instead, it is a bounded, closed, and convex subset in \mathbb{R}^{m^2} of dimension $m(m-1)/2$ as shown in [Proposition 1](#). To ensure that the random response L generated in our simulation resides in \mathcal{L}_m , one needs to make sure that the off-diagonal entries $-\beta_i, i = 1, \dots, d$ are nonpositive and bounded below as per (P2). The other two properties (P0) and (P1) can be guaranteed by the inverse half vectorization vech^{-1} . To this end, in our simulation $\beta_i, i = 1, \dots, d$ are sampled from beta distributions, which are defined on the interval $(0, 1)$ and whose parameters depend on the uniformly distributed predictor X .

The consistency of global DNR relies on the assumption that the true regression function $m(x)$ is equal to $m_G(x)$ as defined in (7) and (8), respectively. This assumption is satisfied if each entry of the graph Laplacian L is conditionally linear in the predictor X . For the global DNR under the Euclidean square root metric $d_{F,1/2}$, an extra matrix square map F_2 is required to ensure that the global DNR in the metric space (\mathcal{M}_m, d_F) as per (25) with $\alpha = 1/2$ is element-wise linear in X .

	Type	Metric	Setting
I	global DNR	d_F	$m(x) = \text{vech}^{-1}(-x, \dots, -x),$ $L = \text{vech}^{-1}(-\beta_1, \dots, -\beta_d),$ where $\beta_j \stackrel{i.i.d.}{\sim} \text{Beta}(X, 1 - X)$
II	global DNR	$d_{F,1/2}$	$m(x) = P_{\mathcal{L}_m}(F_2(P_{\mathcal{M}_m}(\text{vech}^{-1}(-0.1x, \dots, -0.1x)))),$ $L = F_2(\text{vech}^{-1}(-\beta_1, \dots, -\beta_d)),$ where $\beta_j \stackrel{i.i.d.}{\sim} \text{Beta}(0.1X, 1 - 0.1X)$
III	local DNR	d_F	$m(x) = \text{vech}^{-1}(-\sin(\pi x), \dots, -\sin(\pi x)),$ $L = \text{vech}^{-1}(-\beta_1, \dots, -\beta_d),$ where $\beta_j \stackrel{i.i.d.}{\sim} \text{Beta}(\sin(\pi X), 1 - \sin(\pi X))$
IV	local DNR	$d_{F,1/2}$	$m(x) = P_{\mathcal{L}_m}(F_2(P_{\mathcal{M}_m}(E[F_{1/2}(L) X = x]))),$ $L = \text{vech}^{-1}(-\beta_1, \dots, -\beta_d),$ where $\beta_j \stackrel{i.i.d.}{\sim} \text{Beta}(\sin(\pi X), 1 - \sin(\pi X))$

Table 1: Four different simulation scenarios, where m is the true regression function and L represents the generated random response. The parameters for the beta distributions of the random variables β_j depend on the predictors X as indicated for simulation scenarios I - IV.

We investigated sample sizes $n = 50, 100, 200, 500, 1000$, with $Q = 1000$ Monte Carlo runs for each simulation. In each iteration, random samples of pairs (X_k, L_k) , $k = 1, \dots, n$ were generated by sampling $X_k \sim U(0, 1)$, setting $m = 10$, and following the above procedure. For the q th simulation of a particular sample size, with $\hat{m}_q(x)$ denoting the fitted regression function, the quality of the estimation was measured quantitatively by the integrated squared error (ISE)

$$\text{ISE}_q = \int_0^1 d_F^2(m(x), \hat{m}_q(x)) dx, \quad (42)$$

where $m(x)$ is the true regression function. The average quality of the estimation for the $Q = 1000$ Monte Carlo runs was assessed by the mean integrated squared error (MISE)

$$\text{MISE} = \frac{1}{Q} \sum_{q=1}^Q \int_0^1 d_F^2(m(x), \hat{m}_q(x)) dx. \quad (43)$$

The bandwidths for the local DNR in Scenario III and IV were chosen using a leave-one-out cross-validation criterion.

The ISE for each simulation run and different sample sizes under different simulation scenarios are summarized in the boxplots in Figure 2. Both global DNR and local DNR performed in a similar manner for both the Euclidean metric d_F and the Euclidean square root metric

$d_{F,1/2}$. We observe the decreasing ISE for increasing sample sizes, demonstrating the convergence of DNR to the target under various regression settings. That the asymptotic rates of convergence in Section 4 are fairly accurate even for finite samples can be seen from the scatter plots of $\log(\text{MISE})$ versus $\log(n)$ in Figure 3, which also include the fitted least squares regression line, the slope of which indicates the empirical rate of convergence. Recall that the theoretical rates of convergence under the four simulation scenarios are $O_P(n^{-\frac{1}{2}})$, $O_P(n^{-\frac{1}{2}})$, $O_P(n^{-\frac{2}{5}})$, and $O_P(n^{-\frac{2}{5}})$, respectively, as per (12), (33), (16), and (37) in Section 4. Since MISE in (43) approximates the square distance between the true and fitted regression function, theory predicts that the empirical slopes under the four simulation scenarios should be around -1 , -1 , -0.8 , and -0.8 , respectively, and are observed with values -0.99 , -1.01 , -0.80 , and -0.8 as shown in Figure 3. This remarkable agreement of theory and empirical behavior supports the relevance of the theory and also shows that these rates are empirically optimal.

6 Data Applications

6.1 New York yellow taxi system after COVID-19 outbreak

The yellow and green taxi trip records on pick-up and drop-off dates/times, pick-up and drop-off locations, trip distances, itemized fares, rate types, payment types, and driver-reported passenger counts, collected by New York City Taxi and Limousine Commission (NYC TLC), are publicly available at <https://www1.nyc.gov/site/tlc/about/tlc-trip-record-data.page>. Additionally, NYC Coronavirus Disease 2019 (COVID-19) data are available at <https://github.com/nychealth/coronavirus-data>, where one can find citywide and borough-specific daily counts of probable and confirmed COVID-19 cases in New York City since February 29, 2020. This is the date at which according to the Health Department the COVID-19 outbreak in NYC began. We aim to study the dependence of transport networks constructed from taxi trip records on covariates of interest, including COVID-19 new cases, and a weekend indicator, as travel patterns are well known to differ between weekdays and weekends.

We focus on yellow taxi trip records in the Manhattan area, which has the highest taxi traffic, predominantly provided by yellow taxis, and grouped the 66 taxi zones (excluding islands) as

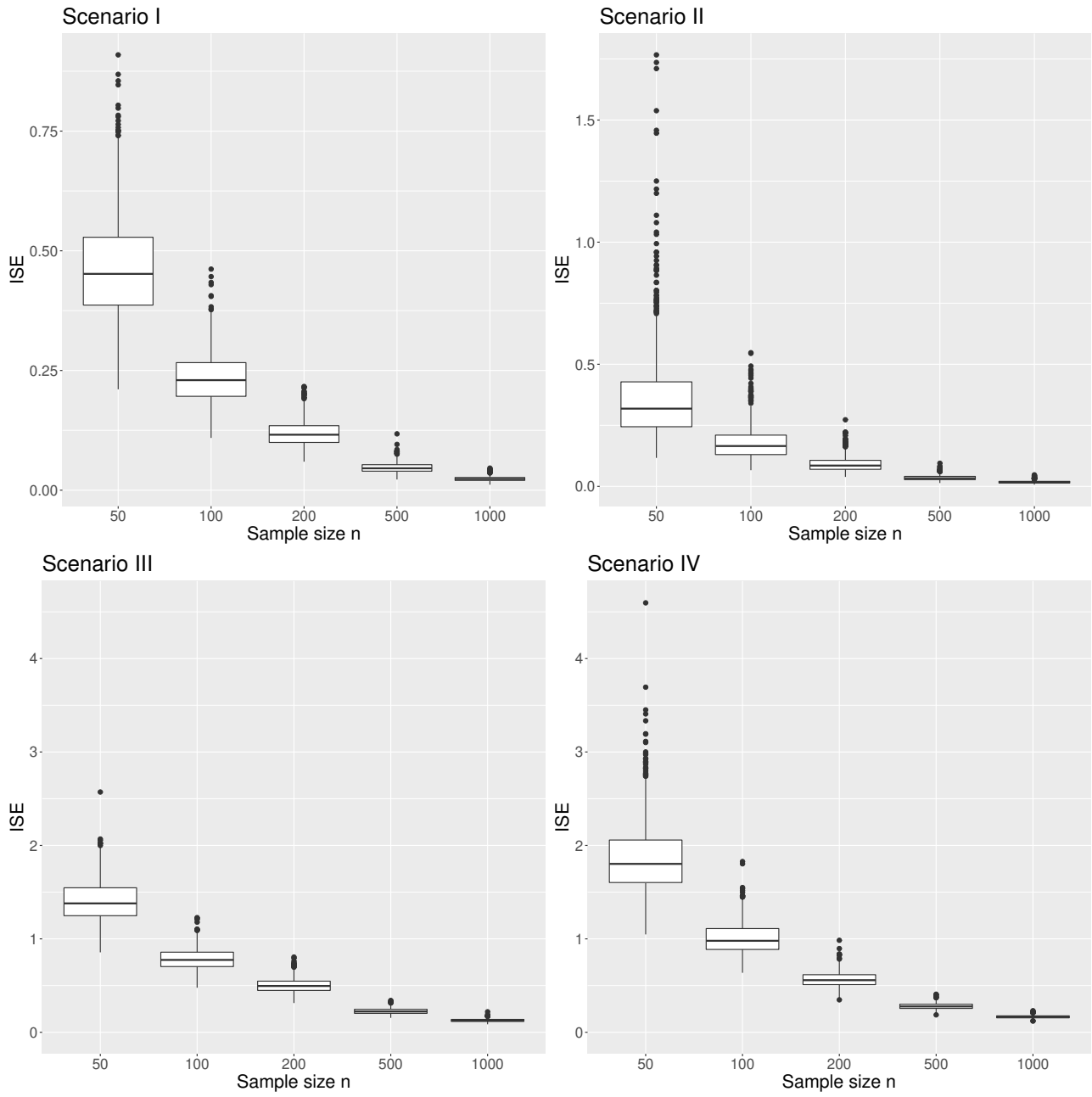


Figure 2: Boxplots of integrated square errors (ISE) for $Q = 1000$ simulation runs and five sample sizes n under four different simulation scenarios.

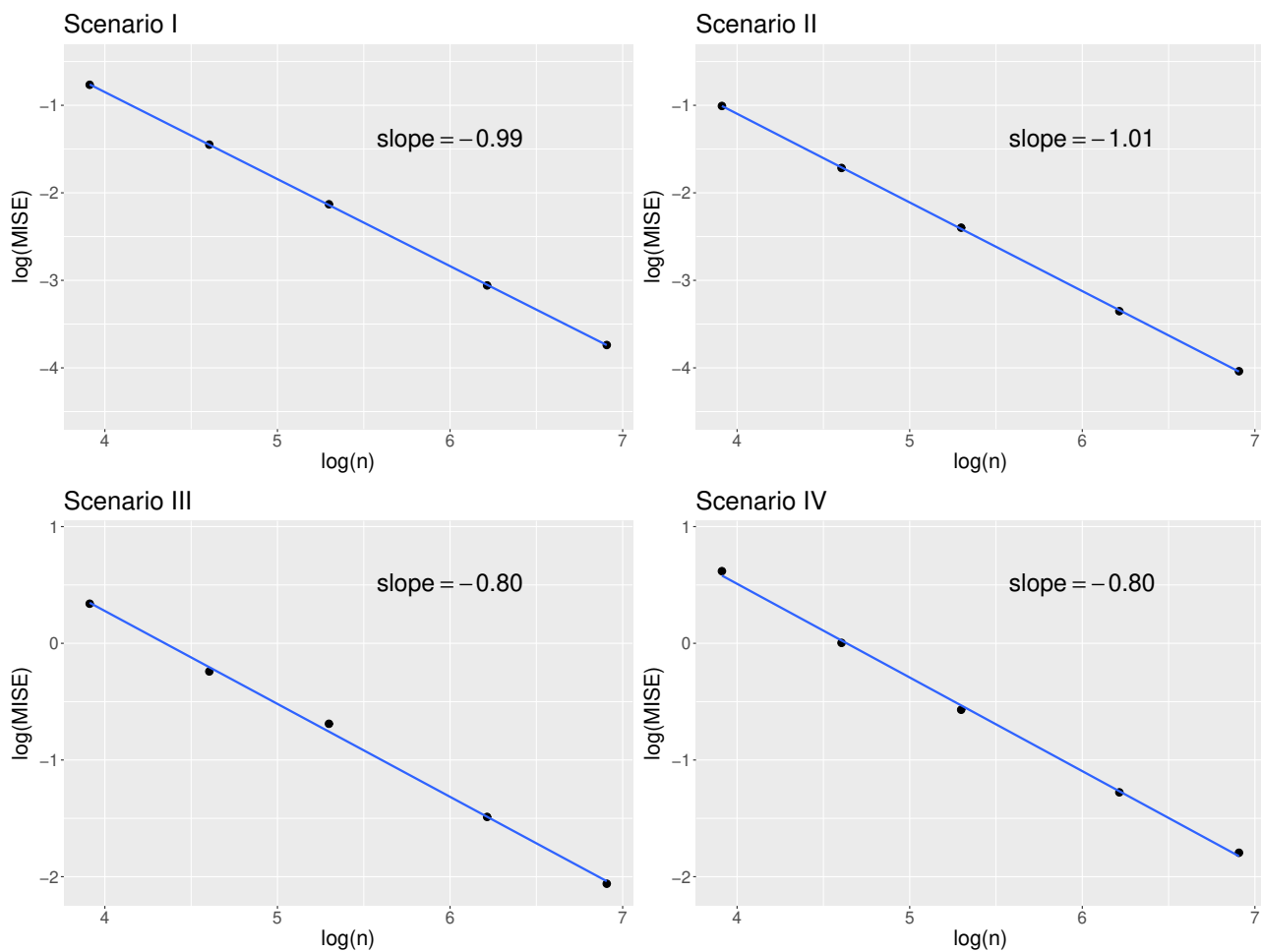
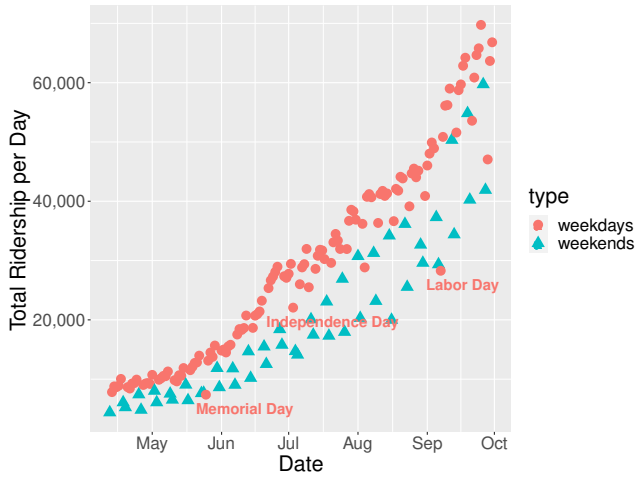


Figure 3: Scatter plots of $\log(\text{MISE})$ versus $\log(n)$ for $Q = 1000$ simulation runs under four different simulation scenarios. Theoretical slopes under the four simulation scenarios are -1 , -1 , -0.8 , and -0.8 , respectively as per Section 4. The empirical rates as sample sizes increase are right on target.

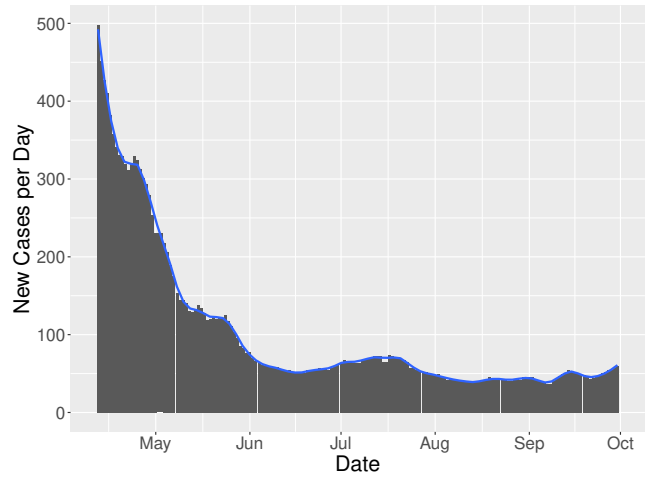
delimited by NYC TLC into 13 regions, which then form the regions of interest. Details about the zones and regions are in Section S.3 of the Supplementary Material. Not long after the outbreak of COVID-19 in Manhattan, yellow taxi ridership, as measured by trips, began a steep decline during the week of March 15, reaching a trough around April 12. This motivated us to restrict our analysis to the time period comprising the 172 days from April 12, 2020 to September 30, 2020, during which yellow taxi ridership per day in Manhattan increased steadily. The total yellow taxi ridership per day is shown in Figure 4(a), where we observe a pronounced difference between weekends and weekdays. Even though the three holidays Memorial Day (May 25), Independence Day (July 3), and Labor Day (September 7) are weekdays, they follow the same travel patterns as weekends, and consequently were classified as weekends in the following analyses.

For each day, we constructed an undirected network with nodes corresponding to the 13 regions and edge weights representing the number of people who traveled between the regions connected by the edges within the day. Since the object of interest is the connection between different regions, we removed self-loops in the networks. We thus have a simple, undirected, weighted network for each of the 172 days from April 12 to September 30. Each of these networks is uniquely associated with a 13×13 graph Laplacian. The covariates of interest include COVID-19 new cases for the day (see Figure 4(b)), and an indicator that is 1 for weekends and 0 otherwise. The first two multi-dimensional scaling (MDS) variables from a classical MDS analysis of the resulting graph Laplacians provide exploratory analysis and are shown in Figure 4(c) and 4(d). These MDS plots indicate that irrespective of the chosen metric, there is a clear separation between weekdays and weekends in MDS2 and that the number of COVID-19 new cases plays an important role in MDS1.

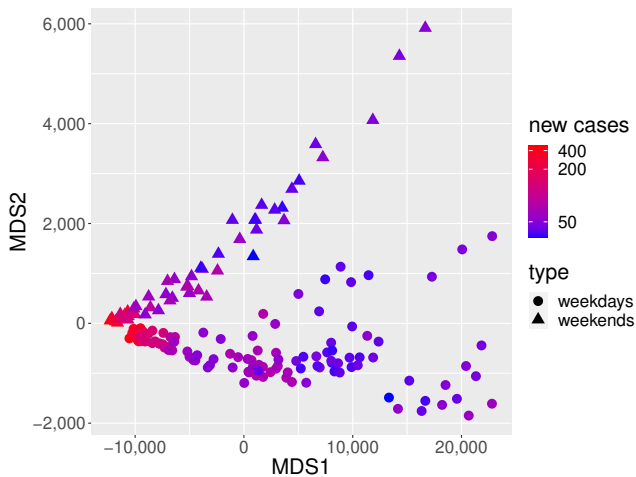
Since the weekend indicator is a binary predictor, we applied global DNR, using both the Euclidean metric d_F and the Euclidean square root metric $d_{F,1/2}$. The estimated mean-square prediction error (MSPE) was calculated for each metric using five-fold cross validation, averaged over 100 runs. A common metric, or which we chose the Euclidean metric d_F , was used to calculate the MSPEs to make them comparable across metrics. The MSPE for $d_{F,1/2}$ was found to be 96.4% of that for d_F , validating the utility of the Euclidean square root metric in real-world applications. Additionally, the Fréchet coefficient of determination $R_{\oplus}^2 = 1 -$



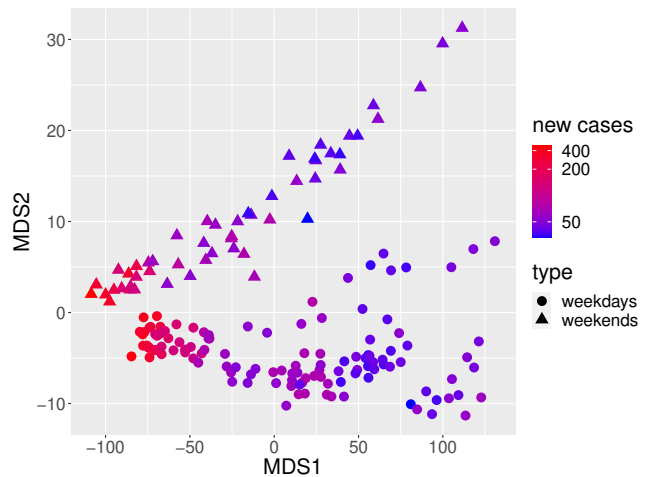
(a)



(b)



(c)



(d)

Figure 4: (a) Total ridership per day in Manhattan, New York. Three holidays Memorial Day (May 25), Independence Day (July 3), and Labor Day (September 7) are highlighted using texts. (b) COVID-19 new cases per day in Manhattan, New York. (c) MDS plot based on the Euclidean metric d_F . (d) MDS plot based on the Euclidean square root metric $d_{F,1/2}$.

$E[d^2(L, m_G(x))]/V_{\oplus}$, an extension of the coefficient of determination R^2 for linear regression, can be similarly used to quantify the proportion of response variation “explained” by the covariates. The corresponding sample version is $\hat{R}_{\oplus}^2 = 1 - \sum d^2(L_k, \hat{m}_G(X_k)) / \sum d^2(L_k, \hat{\omega}_{\oplus})$, where $\hat{\omega}_{\oplus} = \operatorname{argmin}_{\omega \in \mathcal{L}_m} \sum d^2(L_k, \omega)$, and was found to be $\hat{R}_{\oplus}^2 = 0.433$ for d_F and $\hat{R}_{\oplus}^2 = 0.453$ for $d_{F,1/2}$, which further lends support for the use of $d_{F,1/2}$ in this specific application.

True and fitted networks using the Euclidean square root metric $d_{F,1/2}$ for a few days are shown in Figure 5. From top left to bottom right, the four dates were chosen to be spaced evenly in the considered time period April 12 to September 30. For each day, on the left is the observed and on the right the fitted network as obtained from DNR. The size of the nodes indicates the volume of traffic in this region and the thickness of the edges represents their weights. The fitted DNR model is seen to capture both structure and weight information of the networks given relevant covariates, and demonstrates trends that are in line with observations.

To further investigate the effects of COVID-19 new cases and weekends, predicted networks represented as heatmaps at 50, 200, and 400 COVID-19 new cases for weekdays or weekends are shown in Figure 6. Edge weights are seen to decrease for increasing COVID-19 new cases, reflecting the negative impact of the epidemic on the number of people traveling. Additionally, the heatmaps are increasingly concentrated, indicating that movements are getting more limited with increasing numbers of new cases of COVID-19. Weekend taxi traffic, with lighter and less essential traffic compared to weekdays, is more severely affected by COVID-19 and as new cases approach 400 per day comes to a near stop. The regions with the heaviest traffic are 105, 106, 107, and 108, which are chiefly residential areas and include multiple stations and famous tourist attractions, such as Penn Station, Grand Central Terminal, and the Metropolitan Museum of Art.

To better illustrate the effect of COVID-19 new cases and weekends on network structures, Figure 7 shows the same predicted networks but each heatmap has its own color range. This shows that higher case numbers lead to structural changes in traffic more on weekends than on weekdays, likely because weekend travel is more driven by leisure activities and therefore the destinations are more flexible. Blocks involving regions 101, 102, 103 have less traffic with increasing COVID-19 new cases on both weekdays and weekends; these regions are in lower Manhattan — the central borough for business (see Section S.3 of the Supplementary Material),

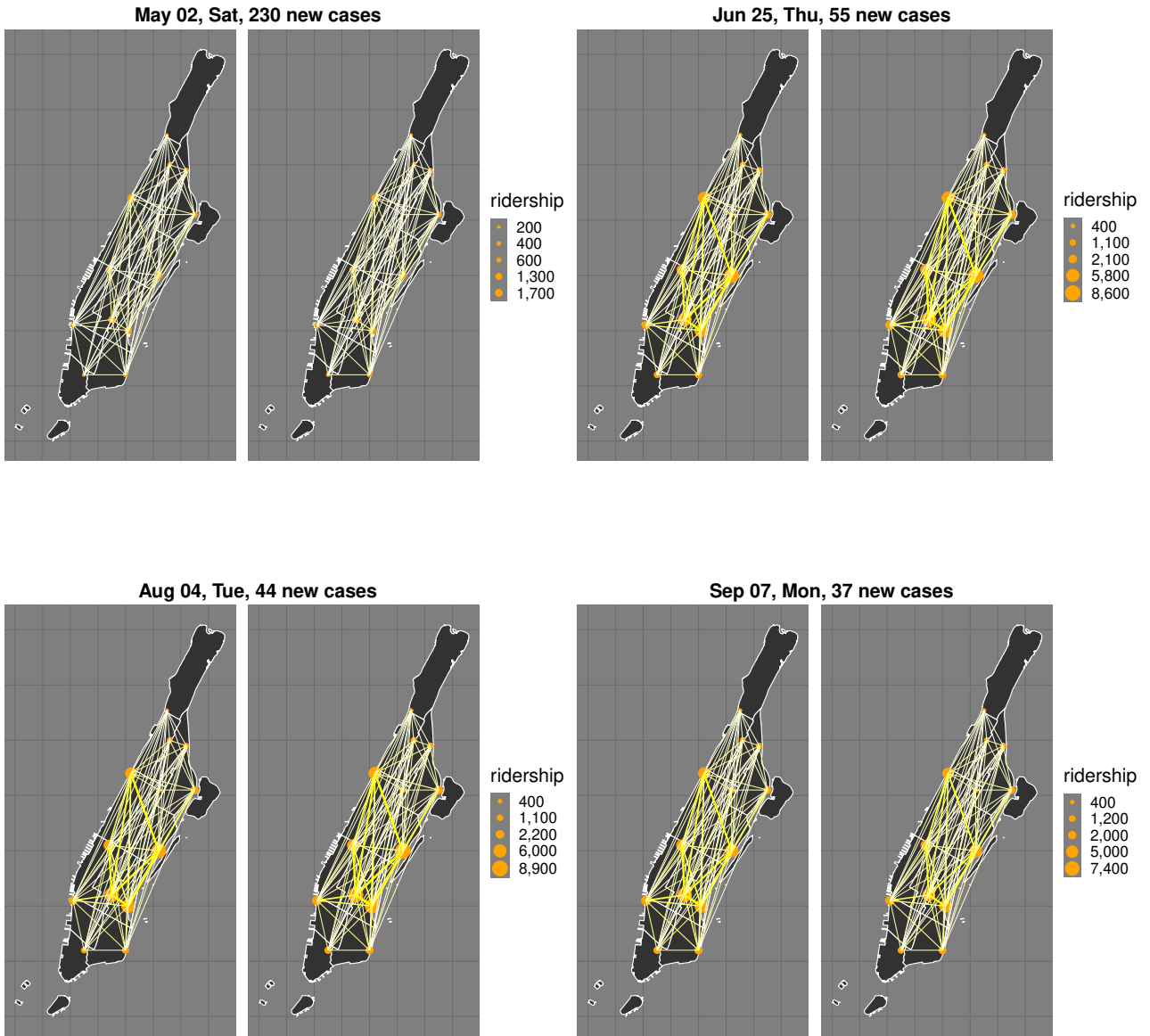


Figure 5: True (left) and fitted (right) networks on May 2, Jun 25, Aug 4, and Sep 7, 2020 (from top left to bottom right). The corresponding days and the number of COVID-19 new cases are in the headline of each subfigure.

which includes the Financial District and the World Trade Center. This likely reflects that more people work from home with increasing case numbers and demonstrates the flexibility of the fits obtained from DNR.

6.2 Dynamics of networks in the aging brain

The increasing availability of neuroimaging data, such as functional magnetic resonance imaging (fMRI) data, has accelerated the investigation of age-related changes in human brain network organization. Resting-state fMRI (rs-fMRI), as an important modality of fMRI data acquisition, has been widely used to study normal aging, which is known to be associated with cognitive decline, even in individuals without any process of retrogressive disorder ([Ferreira and Busatto 2013](#); [Sala-Llonch et al. 2014, 2015](#)).

fMRI measures brain activity by detecting changes in blood-oxygen-level-dependent (BOLD) signals in the brain across time. During recordings of rs-fMRI subjects relax during the sequential acquisition of fMRI scans. Spontaneous fluctuations in brain activity during rest is reflected by low-frequency oscillations of the BOLD signal, recorded as voxel-specific time series of activation strength. Network-based analyses of brain functional connectivity at the subject level typically rely on a specific spatial parcellation of the brain into a set of regions of interest (ROIs) ([Bullmore and Sporns 2009](#)). Temporal coherence between pairwise ROIs is usually measured by so-called temporal Pearson correlation coefficients (PCC) of the fMRI time series, forming a $m \times m$ correlation matrix when considering m distinct ROIs, which can be viewed as a basic measurement of functional connectivity. Hard or soft thresholding ([Schwarz and McGonigle 2011](#)) is customarily applied to produce a binary or weighted functional connectivity network.

Based on the functional connectivity network, the most commonly used network measures of functional connectivity, reflecting centrality of individual brain regions, integration, and segregation, etc., can be derived ([Rubinov and Sporns 2010](#)). Among these, clustering coefficient, characteristic path length and small-worldness are key global topological measures that are widely used in the literature ([Onoda and Yamaguchi 2013](#); [Sala-Llonch et al. 2014](#)). The clustering coefficient is a measure of the cliquishness of connections between nodes from a topological point of view, indicating the extent of local interconnectivity in a network. The

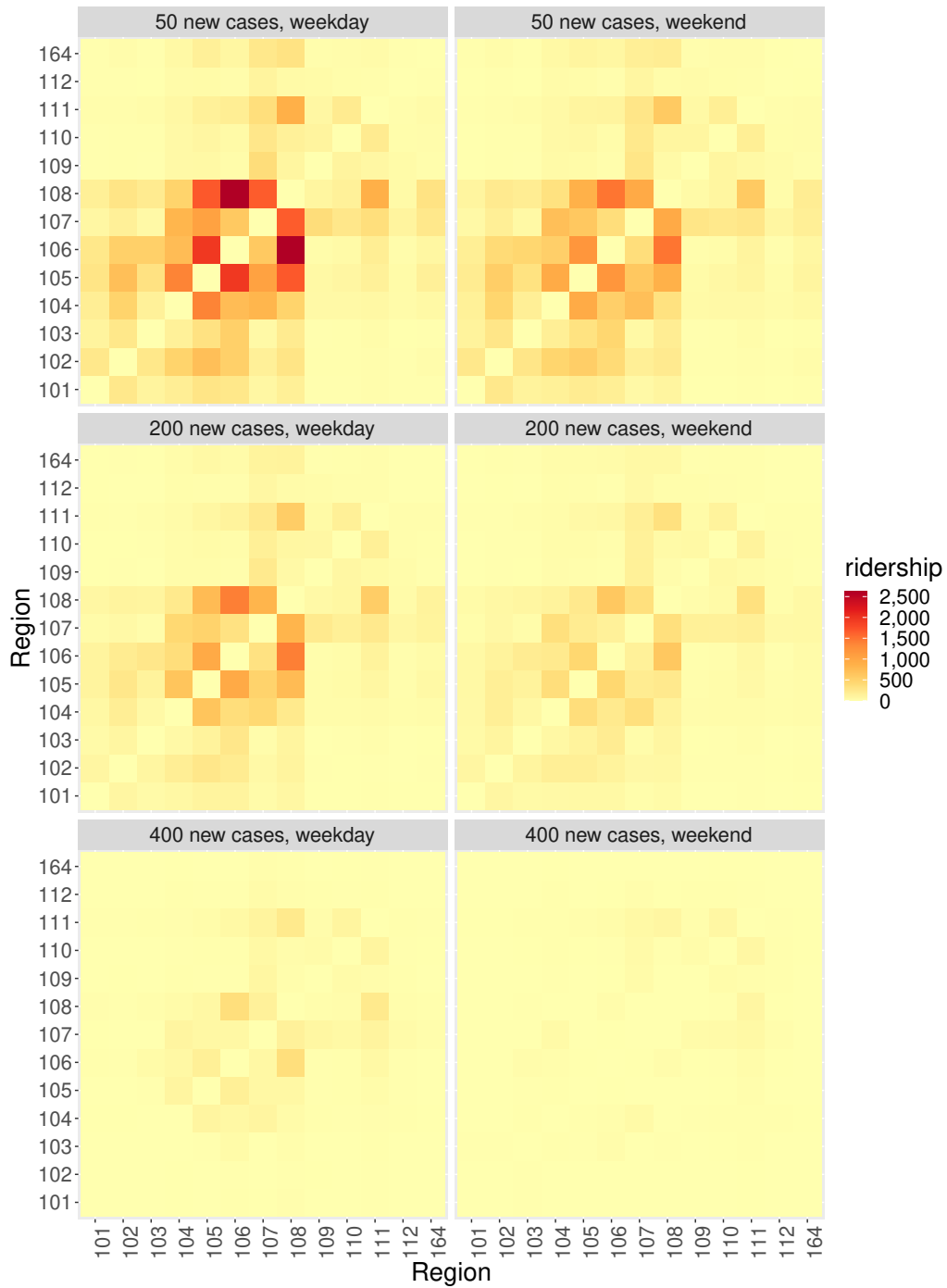


Figure 6: Predicted networks represented as heatmaps at different number of COVID-19 new cases on weekdays or weekends. The top, middle, and bottom rows show, respectively, the predicted networks at 50, 200, and 400 COVID-19 new cases. The left and right columns depict the predicted networks on weekdays and weekends, respectively.

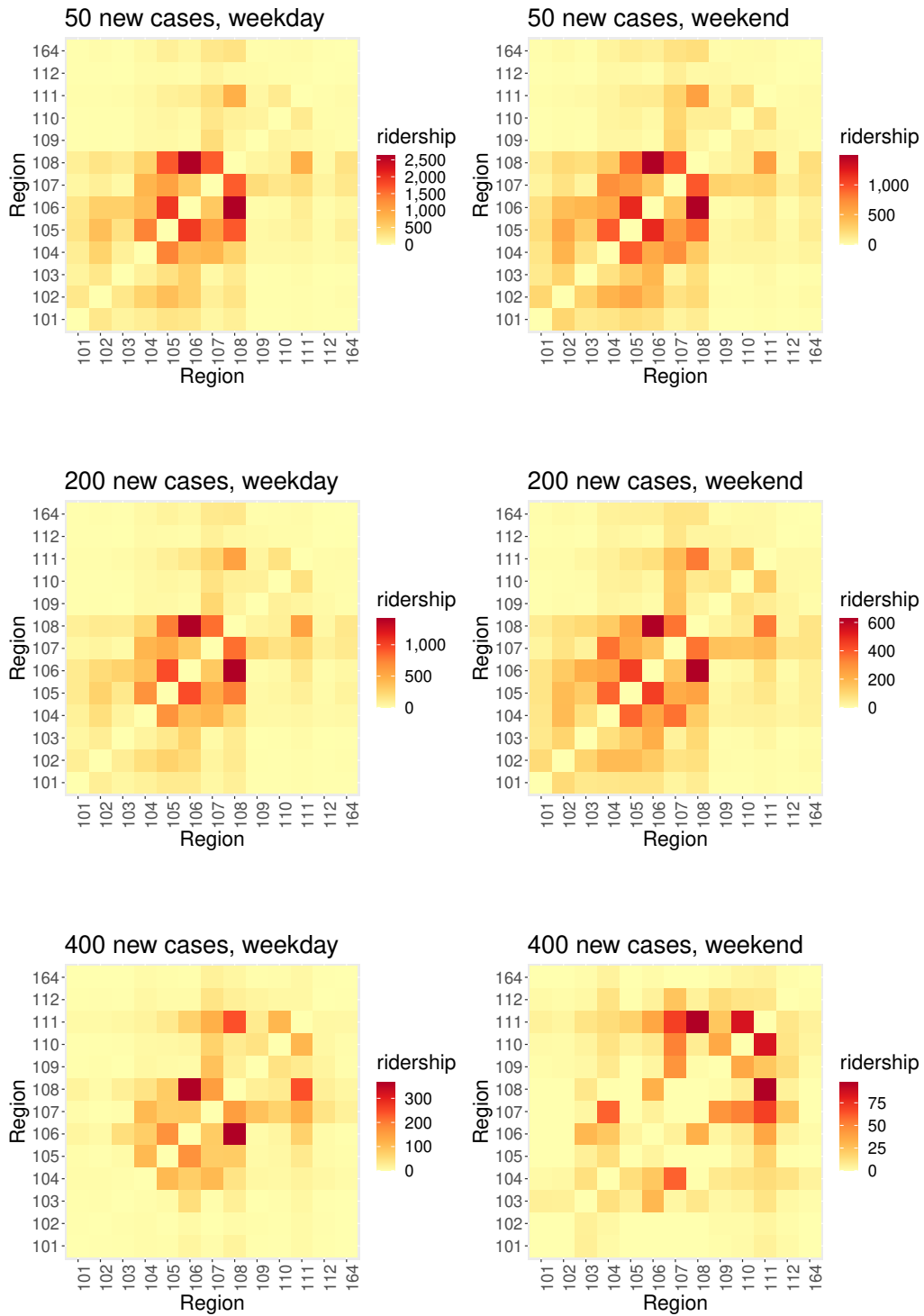


Figure 7: Predicted networks represented as heatmaps at different number of COVID-19 new cases on weekdays or weekends. Each heatmap has its own scale to enhance visualization of changes in connections in dependence on daily COVID-19 new cases. The top, middle, and bottom rows show, respectively, the predicted networks at 50, 200, and 400 COVID-19 new cases. The left and right columns depict the predicted networks on weekdays and weekends, respectively.

characteristic path length quantifies the ability for information to be propagated in parallel, where lower values indicate higher routing efficiency. Small-worldness measures the balance between functional segregation (the presence of functionally specialized modules) and integration (a robust number of intermodular links), indicating the extent of global and local efficiency (Watts and Strogatz 1998).

Local DNR can be employed to investigate healthy aging by modeling the relationship between brain functional connectivity networks and age. One can infer age-related changes in brain network organization based on the dynamics of predicted networks and study the effects of healthy aging in brain network topology using, e.g., clustering coefficient, characteristic path length and small-worldness. Data used in our study were obtained from the Alzheimer’s Disease Neuroimaging Initiative (ADNI) database (adni.loni.usc.edu), where $n = 404$ cognitively normal elderly subjects at ages ranging from 55.61 to 95.39 years old participated in the study; one rs-fMRI scan is randomly selected if multiple scans are available for a subject.

We used the automated anatomical labeling (AAL) atlas (Tzourio-Mazoyer et al. 2002) to parcellate the whole brain into 90 ROIs, with 45 ROIs in each hemisphere. Details about the ROIs can be found in Section S.4 of the Supplementary Material (Table 3). Preprocessing was carried out in MATLAB using the Statistical Parametric Mapping (SPM12, www.fil.ion.ucl.ac.uk/spm) and Resting-State fMRI Data Analysis Toolkit V1.8 (REST1.8, <http://restfmri.net/forum/?q=rest>). Briefly, this included the removal of any artifacts from head movement, correction for differences in image acquisition time between slices, normalization to the standard space, spatial smoothing, and temporal filtering (bandpass filtering of 0.01-0.1 Hz). The mean time course of the voxels within each ROI was then extracted for network construction. A PCC matrix was calculated for all time course pairs for each subject. These matrices were then converted into simple, undirected, weighted networks by setting diagonal entries to 0 and thresholding the absolute values of the remaining correlations. Since most network theoretic measures are sensitive to variations in the number of edges in a network, we used density-based thresholding (Fornito et al. 2016), where the threshold is allowed to vary from subject to subject to achieve a desired, fixed connection density. Specifically, in our analyses the 15% strongest connections were kept to achieve a density of 0.15 for each subject.

We implemented local DNR with the graph Laplacians corresponding to the networks con-

structured from PCC matrices as responses, with age as scalar-valued covariate. The bandwidth for the age was chosen to minimize the prediction error using a leave-one-out cross-validation criterion, resulting in a bandwidth of $h = 0.20$. Prediction was performed at four different ages: 65, 70, 75, and 80 (approximately the 20%, 40%, 60%, and 80% quantiles of the age distribution of the 404 subjects). The predicted networks are demonstrated in Figure 8, where the nodes were placed using the Fruchterman-Reingold layout algorithm (Fruchterman and Reingold 1991) to achieve optimal visualization. Spectral clustering (Newman 2006) was applied to detect the community structure in each network where different communities are distinguished by different colors. The number of communities for age equals 65, 70, 75, and 80 are 10, 12, 12, and 16, respectively. The communities with no less than 10 nodes are highlighted using colored polygons. These communities are found to be associated with different anatomical regions of the brain (see Table 3 in Section S.4 of the Supplementary Material), where a community is identified as the anatomical region the majority of nodes belong to for situations where it intersects with multiple anatomical regions. As can be seen in Figure 8, the communities associated with the central region, the parietal lobe, and the limbic lobe disintegrate into several small communities with increasing age. This finding suggests age-related increases of local interconnectivity or cliquishness. High cliquishness is known to be associated with reduced capability to rapidly combine specialized information from distributed brain regions, which may contribute to cognitive decline for healthy elderly adults (Sala-Llonch et al. 2015).

We also used global network measures (small-worldness, clustering coefficient, and characteristic path length) to measure age-related changes in brain functional integration and segregation. Specifically, the three measures were computed using the fitted network for each subject. The results are shown in Figure 9. We observe that small-worldness is negatively correlated with increasing age but that this decline was relatively slow, indicating lower global and local efficiency of information processing for healthy elderly adults. As a measure of cliquishness, clustering coefficient increases with increasing age, which coincides with the results in Figure 8. Characteristic path length, however, seems not to change much with age. Additionally, we find that brain functional networks are small-world networks as the small-worldness for each subject is higher than 1 (Achard and Bullmore 2007; Humphries and Gurney 2008).

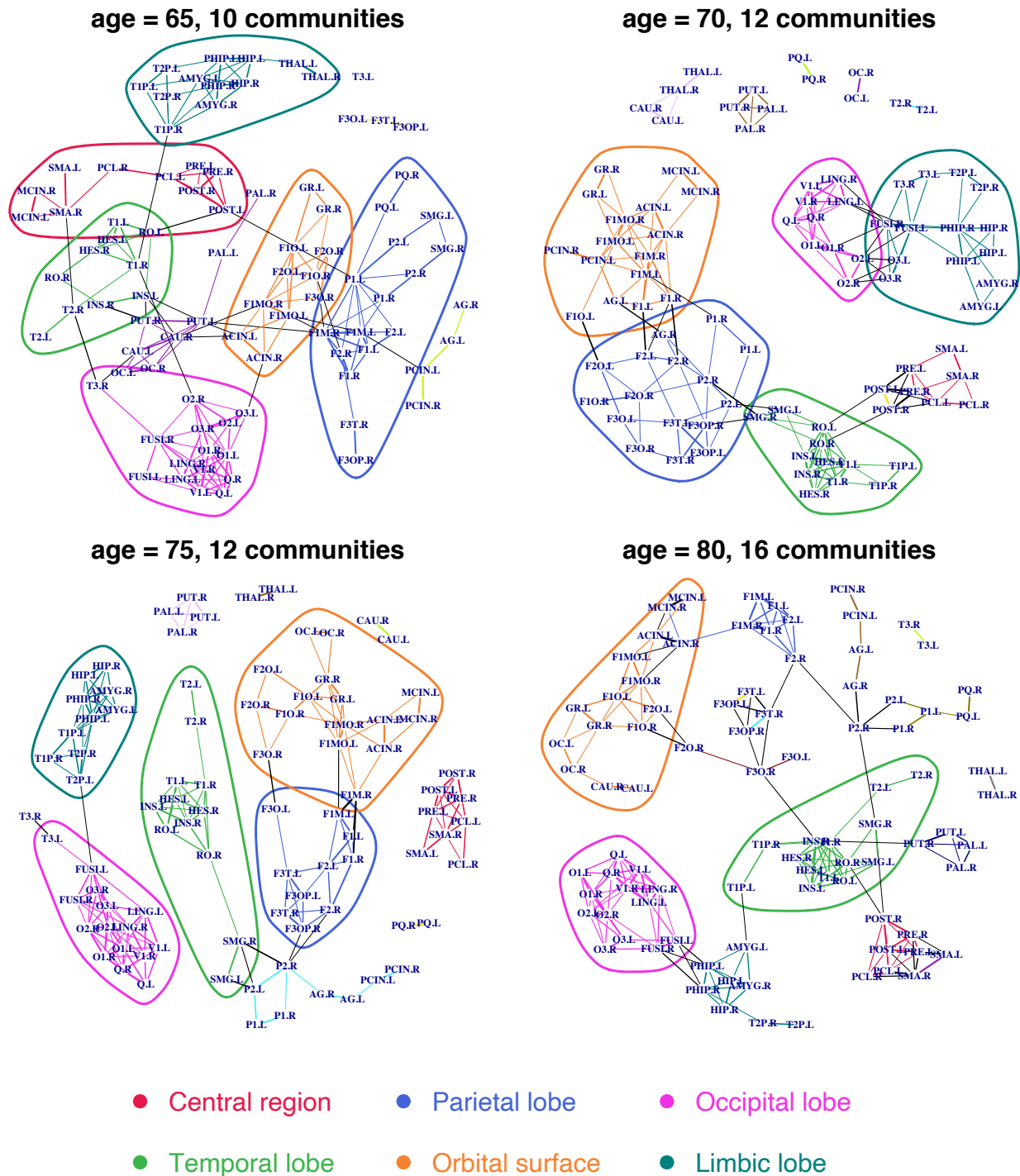


Figure 8: Topological representation using spectral community detection for predicted functional connectivity networks at different ages (years). The communities with no less than 10 ROIs are highlighted using colored polygons. These communities are found to be associated with different anatomical regions of the brain (see Table 3 in Section S.4 of the Supplementary Material).

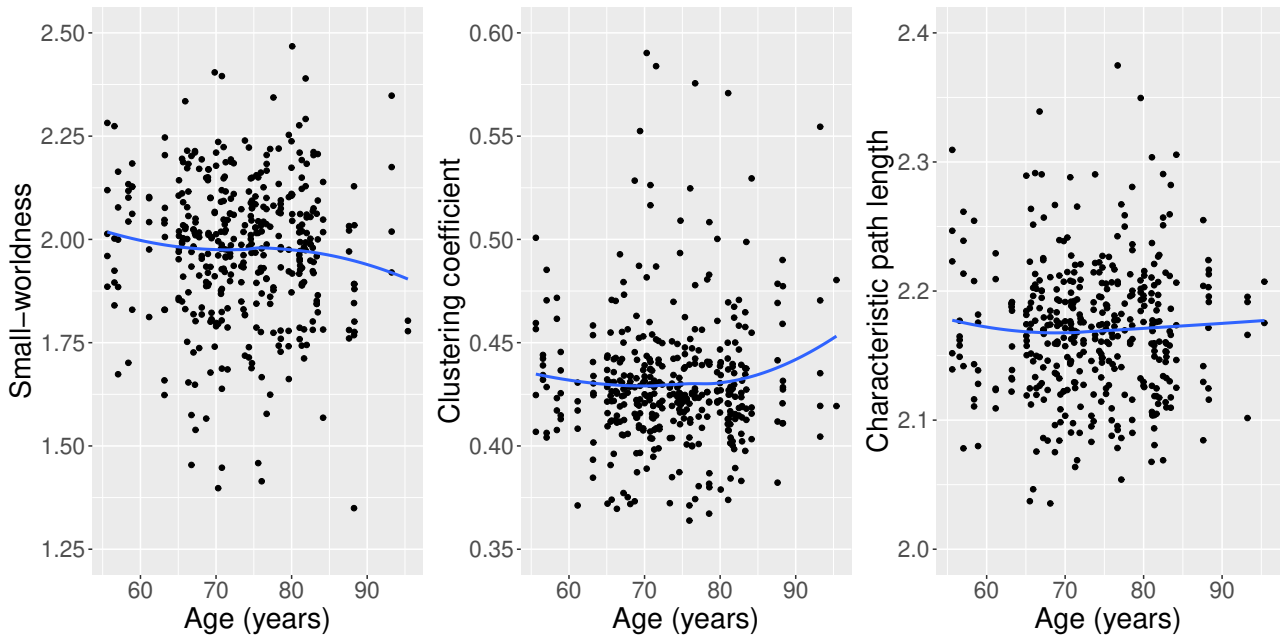


Figure 9: Scatter plots of the correlations between global network measures calculated from fitted networks and age for healthy elderly adults. From left to right: small-worldness, clustering coefficient, and characteristic path length.

Acknowledgements

Data used in this paper were obtained from the Alzheimer’s Disease Neuroimaging Initiative (ADNI) dataset. The investigators within the ADNI did not participate in analysis or writing of this study. A complete list of ADNI investigators can be found online. This research was supported in part through National Science Foundation grant DMS-2014626.

References

- Achard, S. and Bullmore, E. (2007) Efficiency and cost of economical brain functional networks. *PLoS Computational Biology*, **3**, e17.
- Agueh, M. and Carlier, G. (2011) Barycenters in the Wasserstein space. *SIAM Journal on Mathematical Analysis*, **43**, 904–924.
- Arsigny, V., Fillard, P., Pennec, X. and Ayache, N. (2007) Geometric means in a novel vector space structure on symmetric positive-definite matrices. *SIAM Journal on Matrix Analysis and Applications*, **29**, 328–347.

- Bhattacharya, R. and Patrangenaru, V. (2003) Large sample theory of intrinsic and extrinsic sample means on manifolds - I. *Annals of Statistics*, **31**, 1–29.
- (2005) Large sample theory of intrinsic and extrinsic sample means on manifolds - II. *Annals of Statistics*, **33**, 1225–1259.
- Boyd, S., Boyd, S. P. and Vandenberghe, L. (2004) *Convex Optimization*. Cambridge University Press.
- Bullmore, E. and Sporns, O. (2009) Complex brain networks: graph theoretical analysis of structural and functional systems. *Nature Reviews Neuroscience*, **10**, 186–198.
- Calissano, A., Feragen, A. and Vantini, S. (2020) Populations of unlabeled networks: Graph space geometry and geodesic principal components. *MOX Report*.
- (2021) Graph-valued regression: Prediction of unlabelled networks in a non-Euclidean graph-space. *MOX Report*.
- Chen, Y. and Müller, H.-G. (2020) Uniform convergence of local Fréchet regression, with applications to locating extrema and time warping for metric-space valued trajectories. *arXiv:2006.13548*.
- De Klerk, E. (2006) *Aspects of Semidefinite Programming: Interior Point Algorithms and Selected Applications*, vol. 65. Springer Science & Business Media.
- Deutsch, F. R. (2012) *Best Approximation in Inner Product Spaces*. Springer Science & Business Media.
- Dryden, I. L., Koloydenko, A. and Zhou, D. (2009) Non-Euclidean statistics for covariance matrices, with applications to diffusion tensor imaging. *Annals of Applied Statistics*, **3**, 1102–1123.
- Dryden, I. L. and Mardia, K. V. (2016) *Statistical Shape Analysis: with Applications in R*, vol. 995. John Wiley & Sons.
- Dryden, I. L., Pennec, X. and Peyrat, J.-M. (2010) Power Euclidean metrics for covariance matrices with application to diffusion tensor imaging. *arXiv preprint arXiv:1009.3045*.

- Dubey, P. and Müller, H.-G. (2019) Fréchet analysis of variance for random objects. *Biometrika*, **106**, 803–821.
- (2020) Fréchet change-point detection. *Annals of Statistics*, **48**, 3312–3335.
- (2021) Modeling time-varying random objects and dynamic networks. *Journal of the American Statistical Association*, 1–33.
- Ferreira, L. K. and Busatto, G. F. (2013) Resting-state functional connectivity in normal brain aging. *Neuroscience & Biobehavioral Reviews*, **37**, 384–400.
- Fornito, A., Zalesky, A. and Bullmore, E. (2016) *Fundamentals of Brain Network Analysis*. Academic Press.
- Fréchet, M. (1948) Les éléments aléatoires de nature quelconque dans un espace distancié. *Annales de l'institut Henri Poincaré*, **10**, 215–310.
- Fruchterman, T. M. and Reingold, E. M. (1991) Graph drawing by force-directed placement. *Software: Practice and Experience*, **21**, 1129–1164.
- Ginestet, C. E., Li, J., Balachandran, P., Rosenberg, S. and Kolaczyk, E. D. (2017) Hypothesis testing for network data in functional neuroimaging. *Annals of Applied Statistics*, **11**, 725–750.
- Huckemann, S. F. (2012) On the meaning of mean shape: manifold stability, locus and the two sample test. *Annals of the Institute of Statistical Mathematics*, **64**, 1227–1259.
- Humphries, M. D. and Gurney, K. (2008) Network ‘small-world-ness’: a quantitative method for determining canonical network equivalence. *PloS One*, **3**, e0002051.
- Knoke, D. and Yang, S. (2019) *Social Network Analysis*. Sage Publications.
- Kolaczyk, E. D., Lin, L., Rosenberg, S., Walters, J. and Xu, J. (2020) Averages of unlabeled networks: Geometric characterization and asymptotic behavior. *Annals of Statistics*, **48**, 514–538.

- Lin, Z. (2019) Riemannian geometry of symmetric positive definite matrices via Cholesky decomposition. *SIAM Journal on Matrix Analysis and Applications*, **40**, 1353–1370.
- Lyons, R. (2013) Distance covariance in metric spaces. *Annals of Probability*, **41**, 3284–3305.
- Marron, J. S. and Alonso, A. M. (2014) Overview of object oriented data analysis. *Biometrical Journal*, **56**, 732–753.
- Müller, H.-G. (2016) Peter Hall, functional data analysis and random objects. *Annals of Statistics*, **44**, 1867–1887.
- Newman, M. E. (2006) Finding community structure in networks using the eigenvectors of matrices. *Physical Review E*, **74**, 036104.
- Onoda, K. and Yamaguchi, S. (2013) Small-worldness and modularity of the resting-state functional brain network decrease with aging. *Neuroscience Letters*, **556**, 104–108.
- Petersen, A. and Müller, H.-G. (2016) Fréchet integration and adaptive metric selection for interpretable covariances of multivariate functional data. *Biometrika*, **103**, 103–120.
- (2019) Fréchet regression for random objects with Euclidean predictors. *Annals of Statistics*, **47**, 691–719.
- R Core Team (2021) *R: A Language and Environment for Statistical Computing*. R Foundation for Statistical Computing, Vienna, Austria.
- Rubinov, M. and Sporns, O. (2010) Complex network measures of brain connectivity: uses and interpretations. *Neuroimage*, **52**, 1059–1069.
- Sala-Llonch, R., Bartrés-Faz, D. and Junqué, C. (2015) Reorganization of brain networks in aging: a review of functional connectivity studies. *Frontiers in Psychology*, **6**, 663.
- Sala-Llonch, R., Junqué, C., Arenaza-Urquijo, E. M., Vidal-Piñeiro, D., Valls-Pedret, C., Palacios, E. M., Domènech, S., Salvà, A., Bargalló, N. and Bartrés-Faz, D. (2014) Changes in whole-brain functional networks and memory performance in aging. *Neurobiology of Aging*, **35**, 2193–2202.

- Schötz, C. (2020) Regression in nonstandard spaces with Fréchet and geodesic approaches. *arXiv preprint arXiv:2012.13332*.
- Schwarz, A. J. and McGonigle, J. (2011) Negative edges and soft thresholding in complex network analysis of resting state functional connectivity data. *Neuroimage*, **55**, 1132–1146.
- Severn, K. E., Dryden, I. L. and Preston, S. P. (2019) Manifold valued data analysis of samples of networks, with applications in corpus linguistics. *arXiv preprint arXiv:1902.08290*.
- (2021) Non-parametric regression for networks. *Stat*, **10**, e373.
- Stellato, B., Banjac, G., Goulart, P., Bemporad, A. and Boyd, S. (2020) OSQP: an operator splitting solver for quadratic programs. *Mathematical Programming Computation*, **12**, 637–672.
- Sturm, K.-T. (2003) Probability measures on metric spaces of nonpositive curvature. *Heat Kernels and Analysis on Manifolds, Graphs, and Metric Spaces (Paris, 2002)*, **338**, 357–390.
- Tavakoli, S., Pigoli, D., Aston, J. A. D. and Coleman, J. S. (2019) A spatial modeling approach for linguistic object data: Analyzing dialect sound variations across Great Britain. *Journal of the American Statistical Association*, **114**, 1081–1096.
- Tzourio-Mazoyer, N., Landeau, B., Papathanassiou, D., Crivello, F., Etard, O., Delcroix, N., Mazoyer, B. and Joliot, M. (2002) Automated anatomical labeling of activations in SPM using a macroscopic anatomical parcellation of the MNI MRI single-subject brain. *Neuroimage*, **15**, 273–289.
- Von Ferber, C., Holovatch, T., Holovatch, Y. and Palchykov, V. (2009) Public transport networks: empirical analysis and modeling. *The European Physical Journal B*, **68**, 261–275.
- Wang, H. and Marron, J. (2007) Object oriented data analysis: Sets of trees. *Annals of Statistics*, **35**, 1849–1873.
- Wang, Y. R., Li, L., Li, J. J. and Huang, H. (2021) Network modeling in biology: statistical methods for gene and brain networks. *Statistical Science*, **36**, 89–108.

- Watts, D. J. and Strogatz, S. H. (1998) Collective dynamics of ‘small-world’ networks. *Nature*, **393**, 440–442.
- Wihler, T. P. (2009) On the Hölder continuity of matrix functions for normal matrices. *Journal of Inequalities in Pure and Applied Mathematics*, **10**, 1–5.
- Zhou, D., Dryden, I. L., Koloydenko, A. A., Audenaert, K. M. and Bai, L. (2016) Regularisation, interpolation and visualisation of diffusion tensor images using non-Euclidean statistics. *Journal of Applied Statistics*, **43**, 943–978.

Supplemental Material

S.1 Assumptions

To obtain rates of convergence for the global and local DNR estimators, we require the following assumptions that parallel those in [Petersen and Müller \(2019\)](#) and [Chen and Müller \(2020\)](#). For ease of presentation, we replace the graph Laplacian L in global and local DNR introduced in [Section 3](#) by a general random object Y taking values in an arbitrary metric space (Ω, d) and follow the same notations there. Consequently, the following assumptions apply to any random objects taking values in a metric space. We will verify that the two metric spaces, (\mathcal{L}_m, d_F) and (\mathcal{M}_m, d_F) , satisfy these assumptions, which lays the basis for the derivation of rates of convergence for the corresponding estimators.

The following assumptions are required to obtain consistency and rates of convergence of $\hat{m}_G(x)$. For a fixed $x \in \mathbb{R}^p$:

(GP0) The objects $m_G(x)$ and $\hat{m}_G(x)$ exist and are unique, the latter almost surely, and, for any $\varepsilon > 0$,

$$\inf_{d(\omega, m_G(x)) > \varepsilon} M_G(\omega, x) > M_G(m_G(x), x).$$

(GP1) Let $B_\delta(m_G(x)) \subset \Omega$ be the ball of radius δ centered at $m_G(x)$ and $N(\varepsilon, B_\delta(m_G(x)), d)$ be its covering number using balls of size ε . Then

$$\int_0^1 \sqrt{1 + \log N(\delta\varepsilon, B_\delta(m_G(x)), d)} d\varepsilon = O(1) \quad \text{as } \delta \rightarrow 0.$$

(GP2) There exists $\eta_0 > 0$, $C_0 > 0$ and $\gamma_0 > 1$, possibly depending on x , such that

$$\inf_{d(m_G(x), \omega) < \eta_0} \{M_G(\omega, x) - M_G(m_G(x), x) - C_0 d(m_G(x), \omega)^{\gamma_0}\} \geq 0.$$

Uniform convergence results require stronger versions of the above assumptions. Let $\|\cdot\|_E$ be the Euclidean norm on \mathbb{R}^p and $B > 0$ a given constant.

(GU0) Almost surely, for all $\|x\|_E < B$, the objects $m_G(x)$ and $\hat{m}_G(x)$ exist and are unique. Additionally, for any $\varepsilon > 0$,

$$\inf_{\|x\|_E \leq B} \inf_{d(m_G(x), \omega) > \varepsilon} M_G(\omega, x) > M_G(m_G(x), x)$$

and there exists $\zeta = \zeta(\varepsilon) > 0$ such that

$$P\left(\inf_{\|x\|_E \leq B} \inf_{d(\hat{m}_G(x), \omega) > \varepsilon} \{\hat{M}_G(\omega, x) - \hat{M}_G(\hat{m}_G(x), x)\} \geq \zeta\right) \rightarrow 1.$$

(GU1) With $B_\delta(m_G(x))$ and $N(\varepsilon, B_\delta(m_G(x)), d)$ as in (GP1),

$$\int_0^1 \sup_{\|x\|_E \leq B} \sqrt{1 + \log N(\delta\varepsilon, B_\delta(m_G(x)), d)} d\varepsilon = O(1) \quad \text{as } \delta \rightarrow 0.$$

(GU2) There exist $\tau_0 > 0$, $D_0 > 0$, and $\rho_0 > 1$, possibly depending on B , such that

$$\inf_{\|x\|_E \leq B} \inf_{d(m_G(x), \omega) < \tau_0} \{M_G(\omega, x) - M_G(m_G(x), x) - D_0 d(m_G(x), \omega)^{\rho_0}\} \geq 0.$$

We require the following assumptions to obtain pointwise rates of convergence for $\hat{m}_{L,n}(x)$. For simplicity, we assume that the marginal density $f_X(\cdot)$ of X has unbounded support, and consider $x \in \mathbb{R}$ with $f_X(x) > 0$.

(LP0) The kernel $K(\cdot)$ is a probability density function, symmetric around zero. Furthermore, defining $K_{kj} = \int_{\mathbb{R}} K^k(u) u^j du$, $|K_{14}|$ and $|K_{26}|$ are both finite.

(LP1) The marginal density $f_X(\cdot)$ of X and the conditional densities $f_{X|Y}(\cdot, y)$ of X given $Y = y$, exist and are twice continuously differentiable, the latter for all $y \in \Omega$, and $\sup_{x,y} |(\partial^2 f_{X|Y} / \partial x^2)(x, y)| < \infty$. Additionally, for any open set $U \subset \Omega$, $\int_U dF_{Y|X}(x, y)$ is continuous as a function of x .

(LP2) The minimizers $m(x)$, $m_{L,h}(x)$ and $\hat{m}_{L,n}(x)$ exist and are unique, the last almost surely. Additionally, for any $\varepsilon > 0$,

$$\inf_{d(m(x), \omega) > \varepsilon} \{M(\omega, x) - M(m(x), x)\} > 0,$$

$$\liminf_{h \rightarrow 0} \inf_{d(m_{L,h}(x), \omega) > \varepsilon} \{M_{L,h}(\omega, x) - M_{L,h}(m_{L,h}(x), x)\} > 0.$$

(LP3) Let $B_\delta(m(x)) \subset \Omega$ be the ball of radius δ centered at $m(x)$ and $N(\varepsilon, B_\delta(m(x)), d)$ be its covering number using balls of size ε . Then

$$\int_0^1 \sqrt{1 + \log N(\delta\varepsilon, B_\delta(m(x)), d)} d\varepsilon = O(1) \quad \text{as } \delta \rightarrow 0.$$

(LP4) There exists $\eta_1, \eta_2 > 0, C_1, C_2 > 0$ and $\gamma_1, \gamma_2 > 1$ such that

$$\inf_{d(m(x), \omega) < \eta_1} \{M(\omega, x) - M(m(x), x) - C_1 d(m(x), \omega)^{\gamma_1}\} \geq 0,$$

$$\liminf_{h \rightarrow 0} \inf_{d(m_{L,h}(x), \omega) < \eta_2} \{M_{L,h}(\omega, x) - M_{L,h}(m_{L,h}(x), x) - C_2 d(m_{L,h}(x), \omega)^{\gamma_2}\} \geq 0.$$

Obtaining uniform rates of convergence for local DNR is more involved and requires stronger assumptions. Suppose \mathcal{T} is a closed interval in \mathbb{R} . Denote the interior of \mathcal{T} by \mathcal{T}° .

(LU0) The kernel $K(\cdot)$ is a probability density function, symmetric around zero, and uniformly continuous on \mathbb{R} . Furthermore, defining $K_{kj} = \int_{\mathbb{R}} K^k(u) u^j du$, $|K_{14}|$ and $|K_{26}|$ are both finite. The derivative K' exists and is bounded on the support of K , i.e., $\sup_{K(x) > 0} |K'(x)| < \infty$; additionally, $\int_{\mathbb{R}} x^2 |K'(x)| \sqrt{|x \log |x||} dx < \infty$.

(LU1) The marginal density $f_X(\cdot)$ of X and the conditional densities $f_{X|Y}(\cdot, y)$ of X given $Y = y$ both exist and are continuous on \mathcal{T} and twice continuously differentiable on \mathcal{T}° , the latter for all $y \in \Omega$. The marginal density $f_X(\cdot)$ is bounded away from zero on \mathcal{T} , $\inf_{x \in \mathcal{T}} f_X(x) > 0$. The second-order derivative f_X'' is bounded, $\sup_{x \in \mathcal{T}^\circ} |f_X''(x)| < \infty$. The second-order partial derivatives $(\partial^2 f_{X|Y} / \partial x^2)(\cdot, y)$ are uniformly bounded, $\sup_{x \in \mathcal{T}^\circ, y \in \Omega} |(\partial^2 f_{X|Y} / \partial x^2)(x, y)| < \infty$. Additionally, for any open set $U \subset \Omega$, $\int_U dF_{Y|X}(x, y)$ is continuous as a function of x ; for any $x \in \mathcal{T}$, $M(\cdot, x)$ is equicontinuous, i.e.,

$$\limsup_{z \rightarrow x} \sup_{\omega \in \Omega} |M(\omega, z) - M(\omega, x)| = 0. \quad (44)$$

(LU2) For all $x \in \mathcal{T}$, the minimizers $m(x)$, $m_{L,h}(x)$ and $\hat{m}_{L,n}(x)$ exist and are unique, the last almost surely. Additionally, for any $\varepsilon > 0$,

$$\inf_{x \in \mathcal{T}} \inf_{d(m(x), \omega) > \varepsilon} \{M(\omega, x) - M(m(x), x)\} > 0,$$

$$\liminf_{h \rightarrow 0} \inf_{x \in \mathcal{T}} \inf_{d(m_{L,h}(x), \omega) > \varepsilon} \{M_{L,h}(\omega, x) - M_{L,h}(m_{L,h}(x), x)\} > 0,$$

and there exists $\zeta = \zeta(\varepsilon) > 0$ such that

$$P(\inf_{x \in \mathcal{T}} \inf_{d(\hat{m}_{L,n}(x), \omega) > \varepsilon} \{\hat{M}_{L,n}(\omega, x) - \hat{M}_{L,n}(\hat{m}_{L,n}(x), x)\} \geq \zeta) \rightarrow 1.$$

(LU3) With $B_\delta(m(x)) \subset \Omega$ and $N(\varepsilon, B_\delta(m(x)), d)$ as in (LP3),

$$\int_0^1 \sup_{x \in \mathcal{T}} \sqrt{1 + \log N(\delta\varepsilon, B_\delta(m(x)), d)} d\varepsilon = O(1) \quad \text{as } \delta \rightarrow 0.$$

(LU4) There exists $\tau_1, \tau_2 > 0$, $D_1, D_2 > 0$ and $\rho_1, \rho_2 > 1$ such that

$$\inf_{x \in \mathcal{T}} \inf_{d(m(x), \omega) < \tau_1} \{M(\omega, x) - M(m(x), x) - D_1 d(m(x), \omega)^{\rho_1}\} \geq 0,$$

$$\liminf_{h \rightarrow 0} \inf_{x \in \mathcal{T}} \inf_{d(m_{L,h}(x), \omega) < \tau_2} \{M_{L,h}(\omega, x) - M_{L,h}(m_{L,h}(x), x) - D_2 d(m_{L,h}(x), \omega)^{\rho_2}\} \geq 0.$$

S.2 Proofs

Proof of Proposition 1

Proof. Properties (P0) and (P1) can be decomposed into $m(m-1)/2$ and m constraints, respectively. Thus, the dimension of the space of $m \times m$ matrices with properties (P0) and (P1) is $m^2 - m(m-1)/2 - m = m(m-1)/2$, and any matrix satisfying properties (P0) and (P1) is fully determined by its upper (or lower) triangular submatrix. It is easy to verify that properties (P0) and (P1) remain valid under matrix addition and scalar multiplication. Additionally, the matrix consisting of zeros satisfies properties (P0) and (P1). Thus, the space of $m \times m$ matrices with properties (P0) and (P1) is a subspace of \mathbb{R}^{m^2} of dimension $m(m-1)/2$. Thus \mathcal{L}_m can be

bijectionally mapped to the hypercube $\{(x^1, \dots, x^{m(m-1)/2}) : -W \leq x^i \leq 0\}$, which is bounded, closed, and convex. This proves that \mathcal{L}_m is a bounded, closed, and convex subset in \mathbb{R}^{m^2} of dimension $m(m-1)/2$. \square

Proof of Theorem 1 and 2

Proof. Take the response object Y in Section S.1 as the $m \times m$ graph Laplacian L , which resides in \mathcal{L}_m , endowed with the Euclidean metric d_F . We show that the metric space (\mathcal{L}_m, d_F) satisfies assumptions (GP0)–(GP2), (GU0)–(GU2), (LP2)–(LP4) and (LU2)–(LU4). Let $\langle \cdot, \cdot \rangle_F$ be the Frobenius inner product. Define

$$\begin{aligned} B(x) &= E[L|X = x]; \\ B_G(x) &= E[s_G(x)L], \quad \hat{B}_G(x) = n^{-1} \sum_{k=1}^n s_{kG}(x)L_k; \\ B_{L,h}(x) &= E[s_L(x, h)L], \quad \hat{B}_{L,n}(x) = n^{-1} \sum_{k=1}^n s_{kL}(x, h)L_k, \end{aligned}$$

where the expectations and sums for graph Laplacians are element-wise. Since

$$\begin{aligned} M(\omega, x) &= E[d_F^2(L, \omega)|X = x] \\ &= E[d_F^2(L, B(x)) + d_F^2(B(x), \omega) + 2\langle L - B(x), B(x) - \omega \rangle_F | X = x] \\ &= M(B(x), x) + d_F^2(B(x), \omega) + 2E[\langle L - B(x), B(x) - \omega \rangle_F | X = x], \end{aligned}$$

and

$$\begin{aligned} E[\langle L - B(x), B(x) - \omega \rangle_F | X = x] &= \langle E[L|X = x] - B(x), B(x) - \omega \rangle_F \\ &= \langle B(x) - B(x), B(x) - \omega \rangle_F \\ &= 0, \end{aligned}$$

We have

$$M(\omega, x) = M(B(x), x) + d_F^2(B(x), \omega).$$

It follows that

$$m(x) = \operatorname{argmin}_{\omega \in \mathcal{L}_m} M(\omega, x) = \operatorname{argmin}_{\omega \in \mathcal{L}_m} d_F^2(B(x), \omega).$$

Additionally, in view of the facts that

$$\begin{aligned} E[s_G(x)] &= 1, & \frac{1}{n} \sum_{k=1}^n s_{kG}(x) &= 1; \\ E[s_L(x, h)] &= 1, & \frac{1}{n} \sum_{k=1}^n s_{kL}(x, h) &= 1, \end{aligned}$$

we can similarly show that

$$\begin{aligned} m_G(x) &= \operatorname{argmin}_{\omega \in \mathcal{L}_m} M_G(\omega, x) = \operatorname{argmin}_{\omega \in \mathcal{L}_m} d_F^2(B_G(x), \omega), \\ \hat{m}_G(x) &= \operatorname{argmin}_{\omega \in \mathcal{L}_m} \hat{M}_G(\omega, x) = \operatorname{argmin}_{\omega \in \mathcal{L}_m} d_F^2(\hat{B}_G(x), \omega), \\ m_{L,h}(x) &= \operatorname{argmin}_{\omega \in \mathcal{L}_m} M_{L,h}(\omega, x) = \operatorname{argmin}_{\omega \in \mathcal{L}_m} d_F^2(B_{L,h}(x), \omega), \\ \hat{m}_{L,n}(x) &= \operatorname{argmin}_{\omega \in \mathcal{L}_m} \hat{M}_{L,n}(\omega, x) = \operatorname{argmin}_{\omega \in \mathcal{L}_m} d_F^2(\hat{B}_{L,n}(x), \omega). \end{aligned}$$

Then by the convexity and closeness of \mathcal{L}_m , all the minimizers $m(x)$, $m_G(x)$, $\hat{m}_G(x)$, $m_{L,h}(x)$, and $\hat{m}_{L,n}(x)$ exist and are unique for any $x \in \mathbb{R}^p$. Hence (GP0), (GU0) and (LP2), (LU2) are satisfied.

To prove that (GP2), (GU2) and (LP4), (LU4) hold, we note that $m(x)$, viewed as the best approximation of $B(x)$ in \mathcal{L}_m , is characterized by (Deutsch 2012, Chapter 4)

$$\langle B(x) - m(x), \omega - m(x) \rangle_F \leq 0, \quad \text{for all } \omega \in \mathcal{L}_m.$$

It follows that

$$\begin{aligned} M(\omega, x) &= E[d_F^2(L, \omega) | X = x] \\ &= M(m(x), x) + d_F^2(m(x), \omega) + 2E[\langle L - m(x), m(x) - \omega \rangle_F | X = x] \\ &= M(m(x), x) + d_F^2(m(x), \omega) + 2\langle B(x) - m(x), m(x) - \omega \rangle_F \\ &\geq M(m(x), x) + d_F^2(m(x), \omega) \end{aligned}$$

for all $\omega \in \mathcal{L}_m$. Similarly,

$$\begin{aligned} M_G(\omega, x) &\geq M_G(m_G(x), x) + d_F^2(m_G(x), \omega), \\ M_{L,h}(\omega, x) &\geq M_{L,h}(m_{L,h}(x), x) + d_F^2(m_{L,h}(x), \omega), \end{aligned}$$

for all $\omega \in \mathcal{L}_m$. Consequently, we may take η_i and τ_i arbitrary, $C_i = D_i = 1$ and $\gamma_i = \rho_i = 2$ for $i = 0, 1, 2$ in (GP2), (GU2), and (LP4), (LU4).

Next, we show that (GU1) holds, which then implies (GP1). Since \mathcal{L}_m is a subset of \mathbb{R}^{m^2} , for any $\omega \in \mathcal{L}_m$ we have

$$N(\delta\varepsilon, B_\delta(\omega), d_F) = N(\varepsilon, B_1(\omega), d_F) \leq (1 + 2/\varepsilon)^{m^2},$$

Thus, the integral in (GU1) is bounded by

$$\begin{aligned} \int_0^1 \sqrt{1 + m^2 \log(1 + 2/\varepsilon)} d\varepsilon &\leq 1 + m \int_0^1 \sqrt{\log(1 + 2/\varepsilon)} d\varepsilon \\ &\leq 1 + m \int_0^1 \sqrt{\log(3/\varepsilon)} d\varepsilon \\ &= 1 + 3m \int_{\log 3}^\infty \sqrt{y} e^{-y} dy < \infty. \end{aligned}$$

using the substitution $y = \log(3/\varepsilon)$. Since this bound does not depend on δ , (GU1) holds and thus (GP1) as well. Likewise we can show that (LU3) and (LP3) also hold.

Theorem 2 in Petersen and Müller (2019) yields rates of convergence for the global DNR estimator. For the local DNR estimator, rates of convergence can be obtained using Corollary 1 in Petersen and Müller (2019) and Theorem 1 in Chen and Müller (2020). \square

Proof of Proposition 2

Proof. Recall that the matrix power map F_α is defined as

$$F_\alpha(S) = S^\alpha = U\Lambda^\alpha U' : \mathcal{S}_m^+ \mapsto \mathcal{S}_m^+,$$

where $U\Lambda U'$ is the spectral decomposition of S . Specifically, denote the eigenvalues of S by $\lambda_1 \geq \lambda_2 \geq \dots \geq \lambda_m \geq 0$. Then $F_\alpha(S) = U \text{diag}(\lambda_1^\alpha, \lambda_2^\alpha, \dots, \lambda_m^\alpha) U'$. Note that the power function $f(x) = x^\alpha : [0, \infty) \mapsto [0, \infty)$ is $(\alpha, 1)$ -Hölder continuous in $[0, \infty)$ for $0 < \alpha < 1$, and is $\alpha C^{\alpha-1}$ -Lipschitz continuous in $[0, C]$ for $\alpha \geq 1$. Results (1) and (2) follow directly from Theorem 1.1 in Wihler (2009) by choosing the scalar function as the power function $f(x) = x^\alpha$ with $0 < \alpha < 1$ in $[0, \infty)$, and with $\alpha \geq 1$ in $[0, C]$, respectively. \square

Proof of Theorem 3 and 4

Proof. Take the response object Y in Section S.1 as the $m \times m$ bounded symmetric positive semi-definite matrix S , which resides in \mathcal{M}_m , endowed with the Euclidean metric d_F . One can

similarly show that the metric space (\mathcal{M}_m, d_F) satisfies assumptions (GP0)–(GP2), (GU0)–(GU2), (LP2)–(LP4) and (LU2)–(LU4) since \mathcal{M}_m , similar to \mathcal{L}_m , is a bounded, closed, and convex subset in \mathbb{R}^{m^2} . According to Theorem 2 in Petersen and Müller (2019), for the metric space (\mathcal{M}_m, d_F) it holds for $m_G^\alpha(x)$ and $\hat{m}_G^\alpha(x)$ as per (25) and (27) that for a fixed $x \in \mathbb{R}^p$,

$$d_F(m_G^\alpha(x), \hat{m}_G^\alpha(x)) = O_P(n^{-1/2})$$

and for a given $B > 0$,

$$\sup_{\|x\|_E \leq B} d_F(m_G^\alpha(x), \hat{m}_G^\alpha(x)) = O_P(n^{-\frac{1}{2(1+\varepsilon)}}),$$

for any $\varepsilon > 0$.

We now need to derive rates of convergence when we apply the inverse matrix power map $F_{1/\alpha}$ and a projection $P_{\mathcal{L}_m}$ onto \mathcal{L}_m . We consider two cases:

1. $0 < \alpha \leq 1$. By Proposition 2, it holds that

$$\|F_{1/\alpha}(S_1) - F_{1/\alpha}(S_2)\|_F \leq \frac{1}{\alpha} C^{1-\alpha} \|S_1 - S_2\|_F$$

for any $S_1, S_2 \in \mathcal{M}_m$. Hence we have for a fixed $x \in \mathbb{R}^p$,

$$d_F(F_{1/\alpha}(m_G^\alpha(x)), F_{1/\alpha}(\hat{m}_G^\alpha(x))) = O_P(n^{-\frac{1}{2}})$$

and for a given $B > 0$,

$$\sup_{\|x\|_E \leq B} d_F(F_{1/\alpha}(m_G^\alpha(x)), F_{1/\alpha}(\hat{m}_G^\alpha(x))) = O_P(n^{-\frac{1}{2(1+\varepsilon)}}),$$

for any $\varepsilon > 0$.

As shown in the proof for Result 2 in Severn et al. (2019), the projection $P_{\mathcal{L}_m}$ does not increase the distance between two matrices. That is

$$d_F(P_{\mathcal{L}_m}(F_{1/\alpha}(m_G^\alpha(x))), P_{\mathcal{L}_m}(F_{1/\alpha}(\hat{m}_G^\alpha(x)))) \leq d_F(F_{1/\alpha}(m_G^\alpha(x)), F_{1/\alpha}(\hat{m}_G^\alpha(x))).$$

So we deduce that it holds for $m_G(x)$ and $\hat{m}_G(x)$ as per (26) and (28) that for a fixed $x \in \mathbb{R}^p$,

$$d_F(m_G(x), \hat{m}_G(x)) = O_P(n^{-\frac{1}{2}})$$

and for a given $B > 0$,

$$\sup_{\|x\|_E \leq B} d_F(m_G(x), \hat{m}_G(x)) = O_P(n^{-\frac{1}{2(1+\varepsilon)}}),$$

for any $\varepsilon > 0$.

2. $\alpha > 1$:

By Proposition 2, it holds that

$$\|F_{1/\alpha}(S_1) - F_{1/\alpha}(S_2)\|_F \leq m^{\frac{\alpha-1}{2\alpha}} \|S_1 - S_2\|_F^{1/\alpha}$$

for any $S_1, S_2 \in \mathcal{M}_m$. Hence we have for a fixed $x \in \mathbb{R}^p$,

$$d_F(F_{1/\alpha}(m_G^\alpha(x)), F_{1/\alpha}(\hat{m}_G^\alpha(x))) = O_P(n^{-\frac{1}{2\alpha}})$$

and for a given $B > 0$,

$$\sup_{\|x\|_E \leq B} d_F(F_{1/\alpha}(m_G^\alpha(x)), F_{1/\alpha}(\hat{m}_G^\alpha(x))) = O_P(n^{-\frac{1}{2\alpha(1+\varepsilon)}}),$$

for any $\varepsilon > 0$.

By the same argument as in the first case, we deduce that it holds for $m_G(x)$ and $\hat{m}_G(x)$ as per (26) and (28) that for a fixed $x \in \mathbb{R}^p$,

$$d_F(m_G(x), \hat{m}_G(x)) = O_P(n^{-\frac{1}{2\alpha}})$$

and for a given $B > 0$,

$$\sup_{\|x\|_E \leq B} d_F(m_G(x), \hat{m}_G(x)) = O_P(n^{-\frac{1}{2\alpha(1+\varepsilon)}}),$$

for any $\varepsilon > 0$.

Similar arguments apply for the local DNR by combining Proposition 2, Corollary 1 in Petersen and Müller (2019), and Theorem 1 in Chen and Müller (2020). \square

S.3 Taxi zones and regions in Manhattan

The yellow and green taxi trip records on pick-up and drop-off dates/times, pick-up and drop-off locations, trip distances, itemized fares, rate types, payment types, and driver-reported

passenger counts, collected by New York City Taxi and Limousine Commission (NYC TLC), are publicly available at <https://www1.nyc.gov/site/tlc/about/tlc-trip-record-data.page>. The taxi zone map for Manhattan (Figure 10(a)) available at https://www1.nyc.gov/assets/tlc/images/content/pages/about/taxi_zone_map_manhattan.jpg represents the boundaries zones for taxi pick-ups and drop-offs as delimited by the NYC TLC. We excluded the islands (103 Liberty Island, 104 Ellis Island, 105 Governor’s Island) from our study. The remaining 66 zones in Manhattan can be grouped into 13 regions as delimited in Figure 10(b) (source: <https://communityprofiles.planning.nyc.gov>). For the composition of these 13 regions see Table 2.

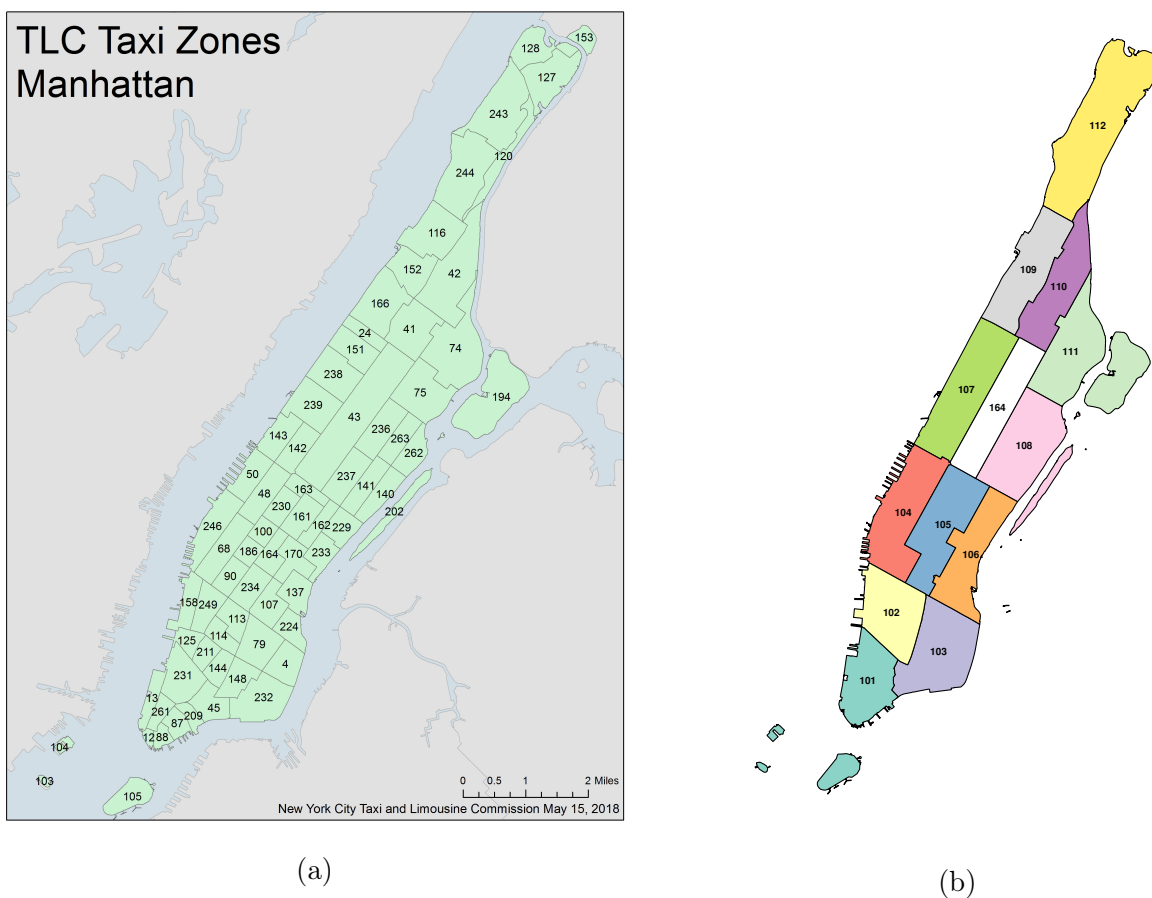


Figure 10: (a) TLC taxi zones in Manhattan, New York. (b) 13 regions in Manhattan, New York.

S.4 Brain regions

These regions are listed in Table 3.

Region	Zones
101	12 Battery Park, 13 Battery Park City, 87 Financial District North, 88 Financial District South, 209 Seaport, 231 TriBeCa/Civic Center, 261 World Trade Center
102	113 Greenwich Village North, 114 Greenwich Village South, 125 Hudson Sq, 144 Little Italy/NoLiTa, 158 Meatpacking/West Village West, 211 SoHo, 249 West Village
103	4 Alphabet City, 45 Chinatown, 79 East Village, 148 Lower East Side, 232 Two Bridges/Seward Park
104	48 Clinton East, 50 Clinton West, 68 East Chelsea, 90 Flatiron, 246 West Chelsea/Hudson Yards
105	100 Garment District, 161 Midtown Center, 163 Midtown North, 164 Midtown South, 186 Penn Station/Madison Sq West, 230 Times Sq/Theatre District, 234 Union Sq
106	107 Gramercy, 137 Kips Bay, 162 Midtown East, 170 Murray Hill, 224 Stuy Town/Peter Cooper Village, 229 Sutton Place/Turtle Bay North, 233 UN/Turtle Bay South
107	24 Bloomingdale, 142 Lincoln Square East, 143 Lincoln Square West, 151 Manhattan Valley, 238 Upper West Side North, 239 Upper West Side South
108	140 Lenox Hill East, 141 Lenox Hill West, 202 Roosevelt Island, 236 Upper East Side North, 237 Upper East Side South, 262 Yorkville East, 263 Yorkville West
109	116 Hamilton Heights, 152 Manhattanville, 166 Morningside Heights
110	41 Central Harlem, 42 Central Harlem North
111	74 East Harlem North, 75 East Harlem South, 194 Randalls Island
112	120 Highbridge Park, 127 Inwood, 128 Inwood Hill Park, 153 Marble Hill, 243 Washington Heights North, 244 Washington Heights South
164	43 Central Park

Table 2: Details about 13 regions in Manhattan, New York.

ROI	Lobe	Label
Central region		
1	Precentral gyrus	PRE
2	Postcentral gyrus	POST
3	Rolandric operculum	RO
Frontal lobe		
Lateral surface		
4	Superior frontal gyrus, dorsolateral	F1
5	Middle frontal gyrus	F2
6	Inferior frontal gyrus, opercular part	F3OP
7	Inferior frontal gyrus, triangular part	F3T
Medial surface		
8	Superior frontal gyrus, medial	F1M
9	Supplementary motor area	SMA
10	Paracentral lobule	PCL
Orbital surface		
11	Superior frontal gyrus, orbital part	F1O
12	Superior frontal gyrus, medial orbital	F1MO
13	Middle frontal gyrus, orbital part	F2O
14	Inferior frontal gyrus, orbital part	F3O
15	Gyrus rectus	GR
16	Olfactory cortex	OC
Temporal lobe		
Lateral surface		
17	Superior temporal gyrus	T1
18	Heschl gyrus	HES
19	Middle temporal gyrus	T2
20	Inferior temporal gyrus	T3
Parietal lobe		
Lateral surface		
21	Superior parietal gyrus	P1
22	Inferior parietal	P2
23	Angular gyrus	AG
24	Supramarginal gyrus	SMG
Medial surface		

25	Precuneus	PQ
Occipital lobe		
Lateral surface		
26	Superior occipital gyrus	O1
27	Middle occipital gyrus	O2
28	Inferior occipital gyrus	O3
Medial surface		
29	Cuneus	Q
30	Calcarine Fissure	V1
31	Lingual gyrus	LING
32	Fusiform gyrus	FUSI
Limbic lobe		
33	Temporal pole: superior temporal gyrus	T1P
34	Temporal pole: middle temporal gyrus	T2P
35	Anterior cingulate and paracingulate gyri	ACIN
36	Median cingulate and paracingulate gyri	MCIN
37	Posterior cingulate gyrus	PCIN
38	Hippocampus	HIP
39	Parahippocampal gyrus	PHIP
40	Insula	INS
Subcortical		
41	Amygdala	AMYG
42	Caudate nuclei	CAU
43	Lenticular nucleus, putamen	PUT
44	Lenticular nucleus, pallidum	PAL
45	Thalamus	THAL

Table 3: Anatomical regions of interest (ROIs) in each hemisphere for the AAL atlas.